

1

Engineering of Coherently Combined, High-Power Laser Systems

Gregory D. Goodno and Joshua E. Rothenberg

1.1

Introduction

In recent years, much effort has been expended toward scaling electric lasers to CW power levels on the order of 100 kW or greater [1]. The key challenge in such scaling is maintaining near-diffraction-limited (DL) beam quality (BQ) to enable tight focusing onto a distant target. Despite the maturation of scalable, diode-pumped laser amplifier technologies such as zigzag slabs [2] or fibers [3], thermal effects or optical nonlinearities currently limit near-DL output from single lasers to an order of magnitude lower power, around 10 kW.

Actively phase-locked coherent beam combination (CBC) of N laser amplifiers seeded by a common master oscillator (MO) represents an engineerable approach toward scaling laser brightness B (loosely defined here as $B \sim \text{power}/\text{BQ}^2$) beyond the limits of the underlying single-element laser technology. Ideally, the combined output behaves as if it were a single beam, and B is thereby increased by a factor of N over an unphased array or by a factor of N^2 over any individual laser [4].

A compelling architectural advantage of CBC systems in comparison to single-aperture lasers of comparable power is the graceful degradation in response to failure of any gain element. This feature can be elucidated from the scaling of $B \sim N^2$, so the relative rate of change in brightness as individual lasers fail is $1/B(dB/dN) = 2/N$. Hence, for large arrays, the drop in brightness is gradual. For example, failure of 1 out of $N = 100$ lasers would still allow a CBC system to continue operating at 98% of its original brightness.

Active CBC with servo-based phase locking can be straightforwardly engineered for very high channel counts and for very high-power laser gain elements. Recently, Northrop Grumman Aerospace Systems adopted an actively phase-locked approach to combine seven 15 kW Nd:YAG slab amplifier chains to demonstrate the world's first 100 kW electric laser with record-setting brightness [5]. As of this writing, work is underway to extend this technology to achieve similar power levels in a CBC array of fiber lasers with improved BQ and efficiency as well as reduced size and weight [6,7].

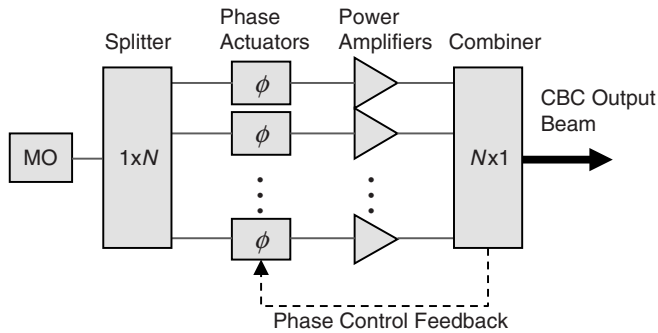


Figure 1.1 System-level block diagram for an actively phase-locked CBC master oscillator power amplifier (MOPA) array.

A canonical system-level architecture for a CBC laser array is shown in Figure 1.1. A single master oscillator is split to seed a number of N channels. Each channel contains a piston phase actuator capable of imposing at least one wave of phase and a coherence-preserving laser amplifier (or a chain of amplifiers) to boost the channel power to the limit of the laser technology. The high-power outputs from all N channels are geometrically combined, so they copropagate, either by using one or more beam splitters or by tiling side by side. The combined output beam is sampled optically to generate error signals for servo-based phase locking of all N channels up to a fraction of a wave.

From Figure 1.1, we can identify three key technologies that must be integrated to form an actively phase-locked, coherently combined, high-power laser system:

- laser amplifiers, preserving coherence properties of a common master oscillator while providing high gain and high output power;
- optical system, geometrically overlapping the amplified beams in the far field (FF) and for some implementations, in the near field (NF); and
- active control systems, cophasing the amplified output beams via closed-loop feedback.

In the remainder of this chapter, we review recent advances in these three technology areas. We begin by deriving engineering requirements on laser source uniformity, presented as trades against combining efficiency. This provides a framework to assess coherent combining technologies amenable to scaling to both high channel counts and high powers, including active piston control using optical heterodyne phase detection and geometric beam combining, using either tiled apertures or diffractive optical elements (DOEs). Finally, we review the engineering challenges, design, and CBC test results of two specific solid-state laser amplifier technologies, Nd:YAG zigzag slabs and Yb:SiO₂ fibers. These laser technologies are particularly well suited toward the demands of 100 kW level CBC owing to their scalability, high gain, high efficiency, and outstanding spatial and temporal coherence properties.

1.2 Coherent Beam Combining System Requirements

The primary requirement for high-efficiency CBC is that the combined beams must be mutually coherent in both space and time to allow complete constructive interference. This means the lasers must be spatially mode-matched and coaligned, power-balanced, copolarized, path length matched, and locked in phase with high precision. When these requirements are not perfectly met, combining efficiency suffers. For a large channel count CBC array, the coherence requirement can be expressed quantitatively and concisely in terms of statistical uniformity tolerances between the laser array elements [8].

We consider a large array of N input beams, combined in a filled aperture configuration using a beam splitter optic in reverse as a beam combiner (BC). This BC can represent, for example, a tapered fiber coupler, a DOE, or a cascade of free space or guided wave splitters. The BC has *a priori* unequal power splitting fractions D_n^2 over the desired channels $n=1-N$, where normalization $\sum_{n=1}^{\infty} D_n^2 = 1$ accounts for the possibility of coupling losses intrinsic to the BC into channels $n > N$ (Figure 1.2). The BC efficiency as a splitter is then $\eta_{\text{split}} = \sum D_n^2$, where the summation is over only the N channels of interest.

Operated as a $N \times 1$ combiner, the spatially resolved, time-averaged combining efficiency $\eta'(x)$ is the ratio of power in the desired output port to the total input power. It is straightforward to show [9] that

$$\eta'(x) = \left\langle \left| \sum D_n E_n(x, t) \right|^2 \right\rangle / \left\langle \sum |E_n(x, t)|^2 \right\rangle. \quad (1.1)$$

Here, the brackets denote time averaging and $E_n(x, t)$ are spatially and temporally nonuniform fields of the input beams. A simple illustration of Eq. (1.1) is shown in Figure 1.3 for the case of $N=2$ beams combined on a 50/50 beam splitter with a small pointing misalignment. Due to the wavefront tilt between beams, the beams cannot interfere constructively over the entire aperture, leading to a spatially varying combining efficiency $\eta'(x)$.

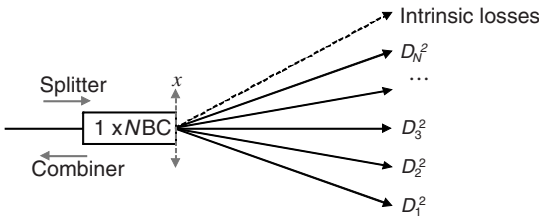


Figure 1.2 Power splitting ratios for a $1 \times N$ beam splitter/combiner.

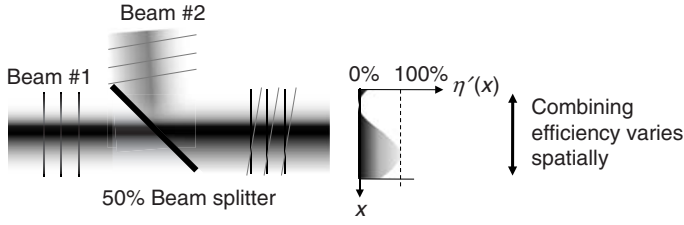


Figure 1.3 Illustration of spatially varying combining efficiency for two misaligned beams combined on a 50% beam splitter.

The overall combining efficiency η is the intensity-weighted average of $\eta'(x)$ over the combining aperture:

$$\eta = \frac{1}{P_{\text{in}}} \int \eta'(x) \langle \sum |E_n(x, t)|^2 \rangle dx = \frac{1}{P_{\text{in}}} \int \left\langle \left| \sum D_n E_n(x, t) \right|^2 \right\rangle dx, \quad (1.2)$$

where $P_{\text{in}} = \int \langle \sum |E_n(x, t)|^2 \rangle dx$ is the total input power (up to a constant). We assume the beams are derived from a common single-mode (SM) CW master oscillator. The MO is assumed to be quasi-monochromatic with carrier frequency ω_0 and slowly time-varying phase modulation $\psi(t)$. Hence, the fields can be written in terms of spatially dependent amplitudes $A_n(x)$ and wavefronts $\phi_n(x)$: $E_n(x, t) = A_n(x) \cos(\chi_n) \exp[i\omega_0 t + i\psi(t) + i\phi_n(x)]$, where χ_n is the depolarization angle of the n th field from the array average.

Since our goal is to identify the effects of relatively small misalignments and aberrations of the input beams, we write each field perturbatively:

$$E_n(x, t) = [A(x) + \delta A_n(x)] (1 - \delta \chi_n^2 / 2) \exp\{i\omega_0(t + \delta \tau_n) + i\psi(t) + i\Delta\omega(t)(t + \delta \tau_n) + i[\phi(x) + \delta \phi_n(x)]\} \quad (1.3)$$

Here, $\delta A_n(x)$ and $\delta \phi_n(x)$ are small deviations of amplitude in the n th field and wavefront distributions from their respective array average, and we have assumed small group delay mismatches $\delta \tau_n$ to allow substitution of the Taylor expansion $\psi(t + \delta \tau_n) \approx \psi(t) + \Delta\omega(t)(t + \delta \tau_n)$, where $\Delta\omega(t) = d\psi(t)/dt$ is a small, time-dependent frequency perturbation. We also assume “quasi-uniform” BC splitting ratios, $D_n = (\eta_{\text{split}}/N)^{1/2} + \delta D_n$, where the amplitude split perturbations are $\delta D_n \ll N^{-1/2}$.

With these approximations, Eq. (1.2) can be evaluated by expanding the exponential, taking the modulus square, and neglecting perturbative terms higher than second order. The resulting expression for efficiency can be written compactly in terms of statistical parameter fluctuations across the array of N beams:

$$\eta = \eta_{\text{split}} \left[1 - (N/P_{\text{in}}) \int \left(\sigma_{A(x)}^2 + A(x)^2 \sigma_{\phi(x)}^2 - 2\sqrt{N/\eta_{\text{BC}}} A(x) \sigma_{A(x), D} \right) dx - \langle \Delta\omega(t)^2 \rangle \sigma_{\tau}^2 - \sigma_{\chi}^2 - N \sigma_D^2 / \eta_{\text{BC}} \right] \quad (1.4)$$

Here, σ_u^2 represents the mean-square variance of the parameters $u = \{A(x), \phi(x), \tau, D, \chi\}$ across the array and $\sigma_{A(x),D}$ is the covariance of the input field amplitudes $A_n(x)$ with the corresponding splitting amplitudes D_n .

In the limit of perfectly coaligned, monochromatic plane waves with a uniform and lossless BC, Eq. (1.4) reduces to

$$\eta = 1 - (\sigma_A/A)^2 - \sigma_\psi^2. \quad (1.5)$$

Equation (1.5) is the well-known Marechal approximation for the effects of amplitude imbalance and piston phase errors between beams [9,10–12]. One should note that since channel power $P \sim A^2$, the relative intensity noise (RIN) variance $(\sigma_P/P)^2 = 4(\sigma_A/A)^2$. Hence, the combining loss due to power imbalance between beams is $(\sigma_P/P)^2/4$ [11,12].

Several useful insights are immediately apparent from Eq. (1.4). First, in the limit of small uncorrelated misalignments, one can independently assess the impact of diverse physical effects such as wavefront errors, power imbalance, and group delay mismatch. The limits of validity of this approximation are illustrated in Figure 1.4 for the simple case of a lossless BC, with no correlation between the input channel powers and BC splitting fractions. The error in the efficiency calculation is $<1\%$ for normalized standard deviations in amplitude of $<20\%$ of the average across the array, corresponding to $<40\%$ variations in input power balance and BC power splitting fractions. Hence, while Eq. (1.4) is an approximation, it nevertheless yields a reliable lower bound on η that is quite accurate for most cases of practical interest (i.e., arrays of similar configuration lasers that are reasonably well aligned).

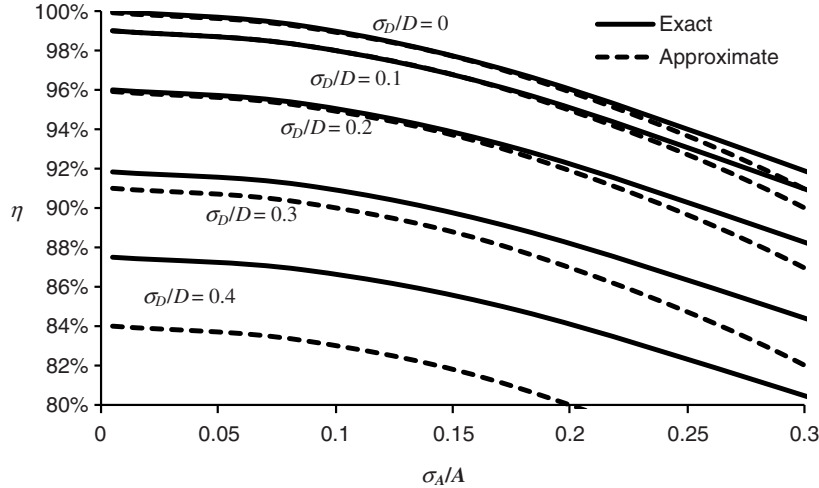


Figure 1.4 Comparison of the approximate [Eq. (1.4)] and exact [Monte Carlo model using Eq. (1.2)] combining efficiencies of large arrays ($N = 10^3$), with normalized standard deviations σ_A/A and σ_D/D of laser amplitude and BC splitting coefficients.

The ability to independently assess varied misalignments using Eq. (1.4) is quite useful toward guiding the design of a CBC laser array, enabling system designers to derive error budgets for the various subsystems and components needed to bring the beams into alignment. In particular, for Gaussian-shaped beams (such as those emitted from single-mode fiber laser amplifiers), Eq. (1.4) results in a very simple analytic expression for CBC loss in terms of Gaussian beam parameters given in Table 1.1. As will be discussed in more detail in the following sections, these expressions have been largely confirmed to be in agreement with experimental measurements of combining efficiency and alignment uniformity of fiber arrays. In general, beams must be spatially coaligned and mode matched to <10% of their Gaussian spot size or coherence length to maintain combining losses below 1%.

It is notable that the loss terms in Eq. (1.4) arise purely from noncommon path (uncorrelated) variations between beams. Adding a common path wavefront to each beam does not change the value of the mean-square variance $\sigma_{\varphi(x)}^2$. Hence, common path wavefront aberrations have no impact on combining efficiency since there is no change in constructive interference between beams. Common wavefront errors can still degrade BQ, since they transmit through the BC onto the combined output.

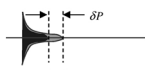
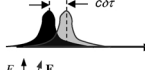
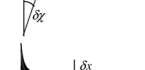
Since the losses in Eq. (1.4) arise purely from uncorrelated aberrations between beams, the CBC process can be seen to serve as an effective “coherent filter.” Whatever fraction of the total input power is successfully combined into the output beam will exhibit substantially reduced wavefront aberration, beam jitter, and phase or frequency noise. The physical intuition is that uncorrelated aberrations captured by the terms in Eq. (1.4) (e.g., pointing jitters, higher order wavefront errors, and nonuniform dispersion) are essentially removed upon coherent combining. This effect is clearly seen in experiments where the far-field pointing jitter and beam quality of the combined beam are in fact improved over the input beams, following a spatial filter to remove the uncombined light that appears outside the diffraction-limited central lobe [2,13]. This is essentially similar physics underlying Fabry–Pérot cavity-based optical mode cleaners [14], with the filter profile defined by the average input field $A(x)e^{i\varphi(x)+i\psi(t)}$ rather than by the modes of a resonant cavity. Due to this coherent filtering effect, CBC appears a promising technology for applications requiring extremely high-quality, high-power beams, such as interferometers for gravity wave detection [15], or resonant cavity-enhanced high-harmonic generation [16].

1.3

Active Phase-Locking Controls

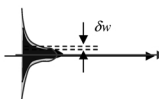
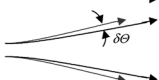
Much of the CBC research literature focuses exclusively on the means by which the lasers are locked in-phase modulo 2π . The advent of commercially available phase actuators based on fiber-coupled, waveguided electro-optic modulators (EOMs) with gigahertz bandwidths and multiwave strokes, coupled with modern RF electronic components and design tools, has resulted in a number of viable control methods, thereby leading a system designer to conduct meaningful trade studies to select the optimum approach for a given CBC system.

Table 1.1 Coalignment and uniformity tolerances for spatially and spectrally aligned Gaussian beams with 1% allowance for combining loss for each effect.

RMS parameter variation	Combining loss, $1 - \eta$	Value for 1% loss	Schematic	Notes
Piston phase, σ_ϕ	σ_ϕ^2	$\sigma_\phi = 0.1$ rad		Also applies to noncommon path, intensity-weighted wavefront aberrations
Power fraction, $\sigma_{\#}P$	$\frac{1}{4}(\sigma_{\#}/P)^2$	$\sigma_{\#}P = 20\%$		$P \sim A^2$, so $\delta P \sim 2\delta A$; hence $\sigma_{\#}P = 2\sigma_A/A$
Optical path mismatch, σ_{τ}	$\frac{\pi^2}{2\ln(2)} \Delta f_{FWHM}^2 \sigma_{\tau}^2$	$\Delta f_{FWHM} = 11$ GHz, $\sigma_{\tau} = 1$ mm		Loss due to dephasing between beams
Polarization angle, σ_x	σ_x^2	$\sigma_x = 0.1$ rad		Equivalent to depolarized power loss
Fractional spot displacement, σ_x/w	$(\sigma_x/w)^2$	$\sigma_x/w = 10\%$		$\delta x =$ beam position error, $w =$ Gaussian beam radius ($1/e^2$ intensity)

(continued)

Table 1.1 (Continued)

RMS parameter variation	Combining loss, $1 - \eta$	Value for 1% loss	Schematic	Notes
Fractional spot size, σ_w/w	$1/2(\sigma_w/w)^2$	$\sigma_w/w = 14\%$		$\delta w =$ beam radius error, $w =$ Gaussian beam radius ($1/e^2$ intensity)
Fractional pointing, σ_θ/θ	$(\sigma_\theta/\theta)^2$	$\sigma_\theta/\theta = 10\%$		$\delta\theta =$ beam pointing error, $\theta =$ Gaussian half-angle divergence ($1/e^2$ intensity)
Fractional divergence, σ_θ/θ	$1/2(\sigma_\theta/\theta)^2$	$\sigma_\theta/\theta = 14\%$		$\delta_\theta =$ divergence error, $\theta =$ Gaussian half-angle divergence ($1/e^2$ intensity)

The BC is assumed to be lossless and uniform ($\eta_{split} = 1$ and $D_n = N^{-1/2}$).

Table 1.2 Comparison of the three major classes of active phase control loops for CBC.

Method	OHD	Synchronous multidither (LOCSET)	Hill climbing
Channel count scaling, N	No limit; fully parallel system	$N = 32$ demonstrated [17]; more appears possible [18]	$N \sim 10$ with ~ 10 kHz control bandwidth
No. of detectors needed	N	1	1
Control bandwidth	> 10 kHz	> 10 kHz	Scales as N^{-1} [19]
Piston set point identification	Manual	Automatic	Automatic
Needs RF electronics?	Yes	Yes	No
Needs optical reference?	Yes	No	No
RMS phase errors	$\lambda/80$ [20]	$\lambda/70$ ($N = 32$) [17]	$\lambda/40$ ($N = 8$) [21]

Shaded cells indicate disadvantages, either with excess system complexity or limited scaling capability.

For a phase locking method to work successfully outside a laboratory environment, it must have an effective control bandwidth of multikilohertz to reject acoustically coupled phase noise and maintain RMS phase stability between channels within $\ll 1$ rad (Table 1.1). Hence, the primary requirement in selecting the phase control method is that it can achieve high-speed and high locking fidelity for the appropriate number of channels N . The most successful phasing methods fall into three broad classes summarized in Table 1.2. We will discuss these three methods in the following sections, concentrating on multichannel optical heterodyne detection (OHD) locking. More detailed descriptions of multidither and hill climbing approaches are presented in Chapters 2, 4, 6, and 8.

1.3.1

Optical Heterodyne Detection

In the OHD method, a reference beam derived from the MO is frequency shifted by $\Delta\omega$ upon passage through an acousto-optic modulator (AOM) before being interferometrically combined with a low-power sample of the beam array using a beam splitter (Figure 1.5). Within each individual beam footprint, a square-law photodetector senses the superimposed fields of the signal and reference beams and produces a time-dependent voltage

$$V(t) = |E_{\text{sig}}|^2 + |E_{\text{ref}}|^2 + 2|E_{\text{sig}}E_{\text{ref}}|\cos[\Delta\omega t + \phi(t)]. \quad (1.6)$$

Here, E_{sig} and E_{ref} are the electric fields of the signal and reference beams and $\phi(t)$ is the time-dependent optical phase jitter between signal and reference beams. OHD can alternatively be implemented in the spatial domain by imposing a tilt (spatial

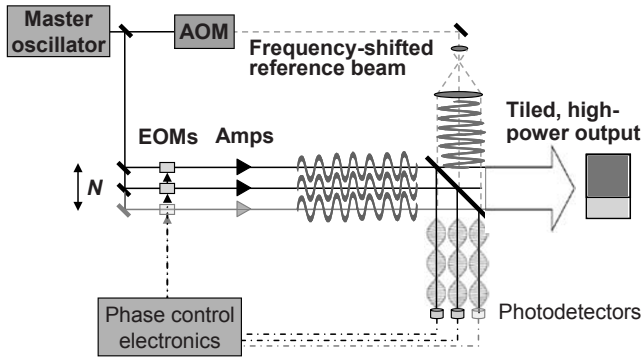


Figure 1.5 Actively phase-locked array of N lasers ($N = 3$ as shown) using the OHD method.

frequency shift) between the signal and reference beams, leading to a spatial interference pattern similar to Eq. (1.6) [22].

From Eq. (1.6), it is apparent that the detector voltage consists of a DC background modulated at the difference frequency owing to interference between the signal and reference beams. This sinusoidal beat waveform is squared up by passing it through a saturated amplifier and is then compared with a similar clock waveform derived from the RF drive voltage to the AOM. The time delay – or phase difference – between the edges of these two waveforms corresponds to the optical phase difference $\phi(t)$ between the signal and reference beams. Applying an exclusive OR function to the clock and heterodyne waveforms as shown in Figure 1.6 results in an output whose area is proportional to $\phi(t)$. This error signal is then fed back to an electro-optic modulator located in the low-power front end of the corresponding amplifier chain to control its phase within a multiple of 2π . In this manner, each beam is locked independently to the same phase as the reference beam and thus indirectly to one another.

The OHD phase locking method has been successfully implemented on numerous fiber- and slab-based laser arrays to demonstrate coherent beam combination [2,5,13,20]. As shown in Figure 1.7, control bandwidths in excess of 10 kHz are readily attainable with this approach, with RMS phase residuals $\sigma_\phi < 0.1$ rad in the presence of phase excursions exceeding 10^4 rad/s. From Eq. (1.5), the consequent CBC loss owing to imperfections in the phase control would be $\sigma_\phi^2 < 1\%$.

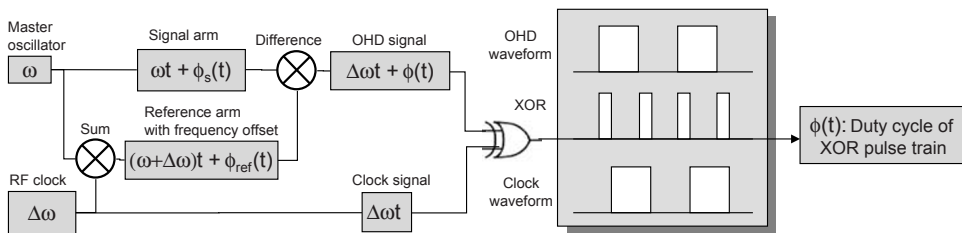


Figure 1.6 XOR logic to generate error signals for the OHD phasing control loop.

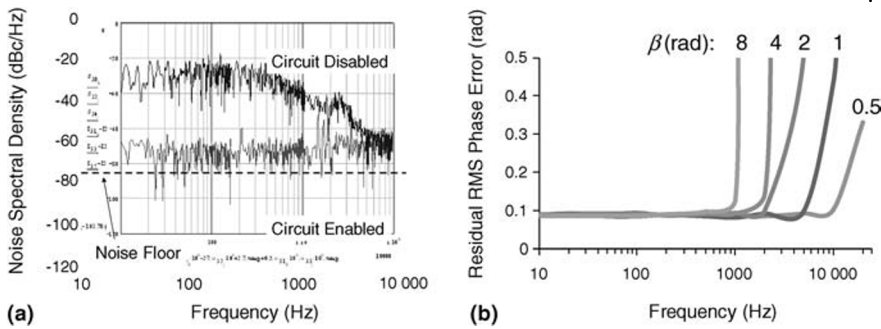


Figure 1.7 OHD phase control loop performance. (a) Noise reduction with OHD loop enabled with a 10 kW Nd:YAG slab amplifier chain [2]. (b) RMS phasing residuals as a function of applied sinusoidal phase noise $\beta \sin(2\pi ft)$ with varying frequency f and amplitude β .

The main benefit of the OHD phasing method is its scalability to large N . All beams are locked directly to a reference, not to each other. Hence, each beam's phase-locking behavior is independent of the presence or absence of other beams. In principle, there is no physical constraint on the number of beams that may be successfully combined.

Since the OHD approach requires one photodetector per beam, it tends to work best in the context of tiled array beam combiners where it is straightforward to overlay an expanded reference beam with a sample of the tiled composite output beam. The method has also been used with filled aperture beam combiners, but it requires reimaging of a common path beam sampled prior to the combiner element [13].

One drawback of the OHD approach is its lack of a direct method to ensure all N beams are locked to one another. Misalignments between the reference and signal beams, drifts in the RF electronics, or static transmissive phase shifts in the main output beam compared to the sampled beam can change the phase-locking set points between beams without changing the RF-detected phase $\phi(t)$. Such misalignments do not impact dynamic phase stabilization, but they do impose static phase errors between beams that must be removed via manual or automated set point adjustment.

1.3.2

Synchronous Multidither

A class of phase locking methods that similar to OHD also utilize heterodyne beats are synchronous multidither approaches and variants thereof [17,18,23–27]. The application of multidither methods for phasing arrays of high-power lasers was fully conceived by the 1970s in the context of atmospheric propagation [23], although the lack of high-speed modulators and sensing electronics severely limited the performance. More recent application of multidither control toward phasing high-power fiber amplifiers has been demonstrated in Ref. [18]. In a multidither phasing system, each laser channel is “tagged” with a small ($\ll 1$ rad) phase dither applied at a unique frequency, typically by superimposing with the control voltage on the EOM

phase controller. A notable variant is the time sharing among channels of a single modulation frequency, with concurrent reduction in control bandwidth [26,27]. A single detector that samples the combined output beam will exhibit a superposition of beats owing to interference between the various beams. Application of standard RF demodulation techniques can extract unique error signals proportional to the phase error between each channel and the rest of the array. These error signals drive servo loops to cophase the beams.

The advantages of multidither are its utilization of a single detector for sensing the phase errors of an entire array and the avoidance of the phase set point ambiguity intrinsic to the OHD method. Minimization of the beat signals in the combined beams corresponds to the condition where all beams are in-phase. The main disadvantage of multidither is its relative electronic complexity and cost, which has at present limited demonstrations to 32 channels [17] despite clear potential for multihundred channel scalability based on signal-to-noise considerations [18].

1.3.3

Hill Climbing

Perhaps the simplest methods for cophasing beams are to maximize the combined power in the far-field central lobe using hill climbing algorithms [19,28], among which the most widely used is the stochastic parallel gradient descent (SPGD) method [29]. In these approaches, the phases of the entire array of beams are simultaneously changed by small, statistically uncorrelated amounts, and the corresponding change in far-field power (or combining efficiency) is sensed. The phase set points are then updated proportionally to the detected change in power, eventually arriving at the maximum power when all beams are in-phase.

Many variants of this class of methods are possible to optimize performance [30,31], but in general hill climbing methods suffer from limited scaling potential since for each added channel, an additional dimension in phase space must be dithered. Consequently, closed-loop bandwidths drop proportionately to $1/N$ [19,21]. Despite this limit, the avoidance of high-speed RF electronics makes this control method relatively low cost and simple to implement using programmable computers. Hence, it is an attractive path for systems with either low channel counts ($N \ll 100$) or low phase noise amplifiers that do not require high-speed phase control [28]. Hill climbing variants with nested loops appear promising to bypass the scaling limitations at some increased cost of complexity [31,32].

1.4

Geometric Beam Combining

In addition to being locked in-phase with high fidelity, the amplified beams must be geometrically overlapped so that they copropagate as a single beam. While the specific optical arrangements can take many forms, the geometric beam combiners in general can be broken into two classes: tiled aperture and filled aperture combiners [4].

1.4.1

Tiled Aperture Combiners

For tiled aperture beam combiners, the amplified beams are positioned side by side in the near field as close together as is feasible without excessive clipping losses. The beams are then pointed in the same direction so that their far fields overlap, synthesizing a composite beam. This approach has the advantage of simplicity and low loss. Moreover, for large arrays, this approach enables the prospect of purely electronic beam steering by controlling the relative phases of each beam, which can be advantageous by eliminating the need for a bulky gimbaled beam director telescope. Finally, since the beam footprints have minimal overlap with one another on optical surfaces, laser-induced damage on one beam footprint allows continued system operation (albeit at reduced efficiency) simply by turning off the beam in question. This lack of single-point failure on the high-power optics can be quite attractive for extremely high-power systems.

The principal drawback of side-by-side beam tiling is that near-field intensity nonuniformity owing to the tiling gaps between beams leads to far-field side lobes in the composite beam. In the limit of large N , the power fraction in the far-field central lobe can be expressed in terms of CBC loss owing to amplitude nonuniformity from Eq. (1.4):

$$1 - P_{\text{side lobes}} = 1 - \frac{N}{P_{\text{in}}} \int \sigma_{A(x)}^2 dx. \quad (1.7)$$

While this term was derived for a filled aperture beam, for a tiled aperture $\int \sigma_{A(x)}^2 dx$ it can be simply reinterpreted as the variance in field amplitude across the composite near field. For the simplified case of flattop near-field beams, Eq. (1.7) reduces to the fill factor of the composite near field. Hence, it is equivalent to the Strehl ratio S or the normalized far-field peak intensity [4]. As the tiled gaps between beams increase, more of the far-field power appears in side lobes away from the diffraction-limited spot size, reducing S and degrading BQ.

If the individual amplified beams have near-flattop intensity profiles, such as those generated from an array of slab lasers (cf., Section 1.5.1), this fill factor impact on BQ can be made arbitrarily small by minimizing the tiling gap between beams [2]. However, when the laser elements are single-mode fiber lasers, which generate near-Gaussian intensity profiles, the loss in BQ of a close-packed tiled array can be substantial. This is illustrated in Figure 1.8 in which only 63% of the power in a coherently combined 2×2 tiled fiber laser array is contained within the diffraction-limited far-field central lobe [20]. The fraction of power in the far-field side lobes can be reduced only by reducing the spacing between beams, which unavoidably reduces the overall combination efficiency owing to near-field clipping of the Gaussian beam wings. Gaussian beams can also be reshaped to a flattened profile with refractive or diffractive optics, but such an approach is limited in effectiveness and also leads to degradation of the beam wavefronts and thus to reduced coherent combination efficiency.

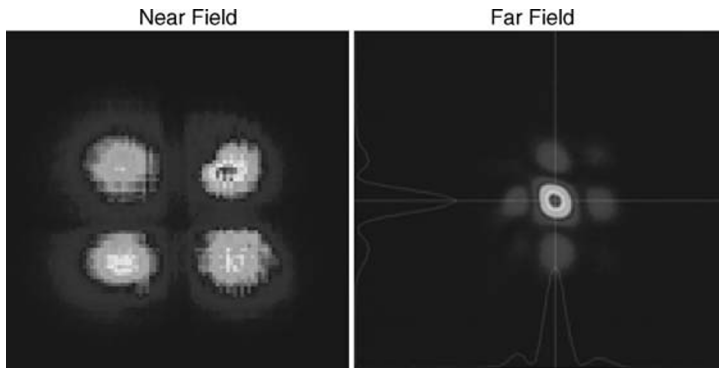


Figure 1.8 Near-field and far-field images of a tiled 2×2 CBC array of close-packed single-mode fiber lasers.

1.4.2

Filled Aperture Combiners Using Diffractive Optical Elements

Filled aperture beam combiners avoid this fill factor limitation by superimposing beams in the near field, using one or more beam splitter elements used in reverse as beam combiners. Examples of such elements are shown in Figure 1.9, and can include cascaded arrays of Fresnel beam splitters [33] or wave plate–polarizer pairs [34,35], tapered fiber couplers (either multichannel [36] or cascaded dual-channel [37]), Talbot-imaged waveguides [38,39], diffractive optical elements [9,13,40], and volume Bragg gratings (VBGs) [41]. As depicted in Figure 1.9, filled aperture combiners can be broadly classified as either free space or guided wave and as either dual-beam ports or multiple beam ports. While guided wave combiners fused to input delivery fibers are interesting for moderate power applications owing to their alignment insensitivity, it appears challenging to scale these components to extremely high ($\gg 10$ kW) powers owing to the high intensities resulting from waveguide confinement. Dual-port combining elements require cascading to

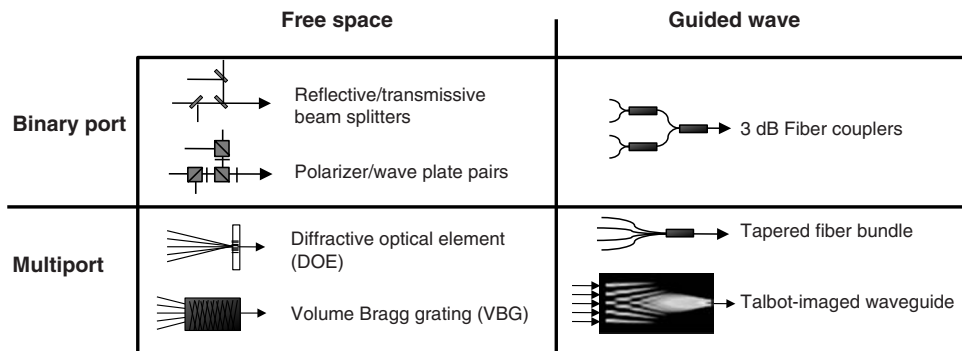


Figure 1.9 Optical configurations for filled aperture beam combining.

combine more than two beams; hence, these approaches tend to be lossy due to both direct transmission losses through each stage of combiner and the CBC losses from accumulated wavefront errors imposed by the upstream combiner elements.

From Figure 1.9, it is apparent that diffractive elements are uniquely well suited toward the demands of high-power, high channel count CBC. By virtue of their multiport and free space nature, both combining efficiency and power handling favorably compare to other filled aperture approaches, all of which involve multiple optical components and/or guided wave interactions. Of the two diffractive, free space–multiport approaches shown in Figure 1.9, power scaling of VBGs appears limited by thermal effects arising from trace absorption on the order of ~ 100 ppm/cm at $1\ \mu\text{m}$ laser wavelengths in the thick photothermorefractive glass medium [42]. In contrast, DOEs rely on a single low-loss optical surface interaction with an order of magnitude less absorption and the ability to be face-cooled from the rear for large-area heat sinking.

1.4.2.1 Overview of DOE Combiners

Used as a beam splitter, a DOE splits an input laser beam into multiple output beams at angles that represent the diffractive orders m of the structure shown in Figure 1.10. Proper design of the phase substructure within the primary DOE period Λ enables fine control over the amplitudes of the m orders, thereby allowing the power to be distributed nearly equally and with high efficiency among a desired number of orders [43]. Since light propagation is reciprocal, the same DOE splitter can also serve as a beam combiner. If mutually coherent beams are incident on the DOE at angles corresponding to the diffractive orders, the beams can constructively interfere to produce a single output beam, provided the phases of the input beams are locked to the correct modulo 2π values determined by the DOE design [9,44]. The combined beam exhibits substantially the same intensity profile as the individual beams, thus eliminating the far-field side lobe structure that is typically observed in tiled composite beam arrangements such as in Figure 1.8. An example of the output order from the CBC of a low-power, five-fiber array using a DOE is shown in Figure 1.11 [13]. The central DOE output order contained 91% of the input power, with the remaining power scattered into higher output orders.

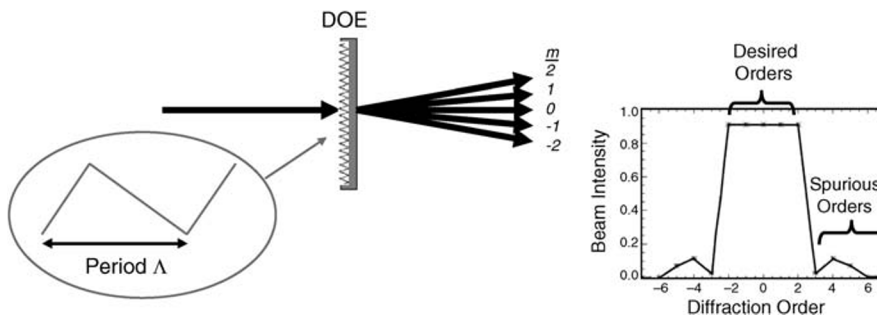


Figure 1.10 DOE periodic surface profiles create multiple grating orders as a splitter. The shape within each period defines the power distribution between orders.

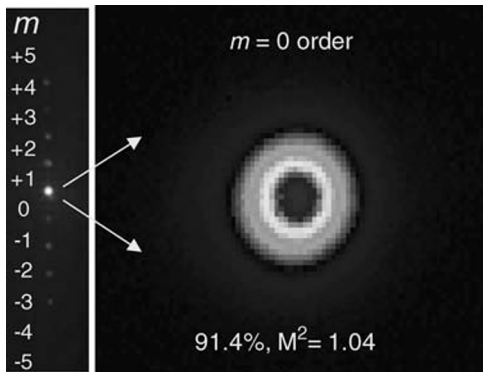


Figure 1.11 Far-field distribution of a five-channel phase-locked fiber array combined using a DOE.

1.4.2.2 DOE Design and Fabrication

Similar to traditional holographic diffraction gratings, DOEs used for CBC are fabricated by etching a continuous surface relief profile into a substrate, typically silicon or fused silica. A variety of DOE designs are possible to accommodate a wide range of channel counts and angular ranges of interest. For a surface relief structure with periodicity Λ and a near-normal incident beam, the diffraction angle θ_m of the m th order is given by the grating equation:

$$\sin(\theta_m) = m\lambda/\Lambda. \quad (1.8)$$

Hence, for a typical $\Lambda \approx 1$ mm DOE period and $\lambda = 1 \mu\text{m}$ wavelength lasers, the angular separation between orders is $\lambda/\Lambda = 1$ mrad.

As illustrated in Figure 1.12, Λ of the DOE surface structures is typically about two orders of magnitude larger than the periods of high-dispersion diffraction gratings used for spectral beam combining (SBC) [45,46]. Consequently, the etched DOE surface is smooth with low aspect ratio. This yields a low-angle

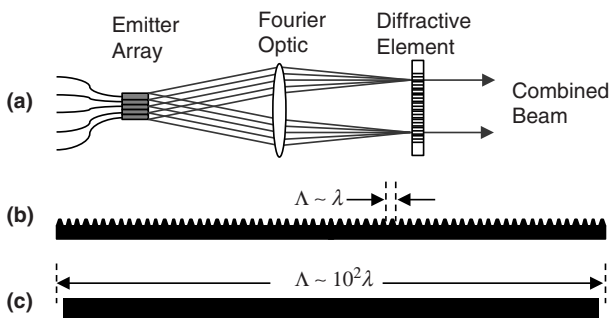


Figure 1.12 (a) Fourier optical configuration for SBC or CBC. (b) Typical surface profile for SBC diffraction gratings, with near-unity aspect ratio. (c) Typical surface profile for CBC DOE (25-beam DOE design shown to scale), with $\sim 3^\circ$ maximum surface slope.

surface profile that is easily coated with a high-quality optical coating, is cleaned with standard methods, and is resistant to thermal effects. Both antireflection (AR) and high-reflection (HR), ultralow absorption, multilayer dielectric coatings with reflectivities of 0.1% (AR) and 99.99% (HR) have been applied to fabricated DOEs without measurably affecting their diffraction properties, indicating that the surface profile is slightly changed by adding the thick dielectric coating stack. The photolithographic processes utilized in fabrication of the surface profile can be straightforwardly applied to substrates 10–15 cm in diameter to accommodate large beam footprints for power scaling with low damage risk.

The intrinsic beam splitter efficiency η_{split} is determined by the DOE design shape and manufacturing tolerances. The beam count N can be defined arbitrarily within the limits of surface shape manufacturing capability. To establish the capability to scale to large beam counts, numerous 1D and 2D DOEs have been designed and fabricated for a variety of channel counts, ranging from $N=3$ to $N=81$ beams with theoretical design values up to $\eta_{\text{split}}=99.4\%$ for $N=9$ (Table 1.3). Manufacturing tolerances are expected to slightly degrade the actual splitter efficiency by single-percent values as illustrated in Figure 1.13. By testing the fabricated DOEs' performance as beam splitters, we verified the capability of the as-fabricated DOEs to match the expected combination efficiency.

It is possible to optimize a DOE combiner design by relaxing the requirement that it split powers equally between the N channels of interest. With unequal power split fractions $|D_n|^2$, the RMS variation σ_D in amplitude transmission coefficients is nonzero. From Eq. (1.4), one can see that the efficiency of the DOE when used as a beam combiner, rather than as a splitter, will depend on the power balance among channels. The optimum case is when the input field amplitudes are perfectly correlated channel by channel with the DOE transmission coefficients ($A_n \propto D_n$). In this case, the loss term in Eq. (1.4) that is proportional to the covariance $\sigma_{A(x),D}$ exactly cancels the loss terms proportional to input power and splitter nonuniformities, $\sigma_{A(x)}^2$ and σ_D^2 . In the absence of any beam

Table 1.3 Examples of DOEs designed for different numbers of beams, showing theoretical splitter efficiencies, along with the expected and as-fabricated efficiency as a combiner with perfectly aligned, equal power input beams.

DOE channel count N	Diffacted beam pattern $N_x \times N_y = N$	Designed splitter efficiency η_{split} (%)	Designed combiner efficiency $\eta_{\text{split}} - N\sigma_D^2$ (%)	As-fabricated combiner efficiency (%)
3	1 × 3	94.9	93.8	93
5	1 × 5	98.0	96.3	95.8
9	1 × 9	99.4	99.3	99.0
15	3 × 5	93.0	90.3	87.8
25	1 × 25	99.4	99.2	98.0
81	1 × 81	99.3	99.2	97
81	9 × 9	98.7	98.6	96

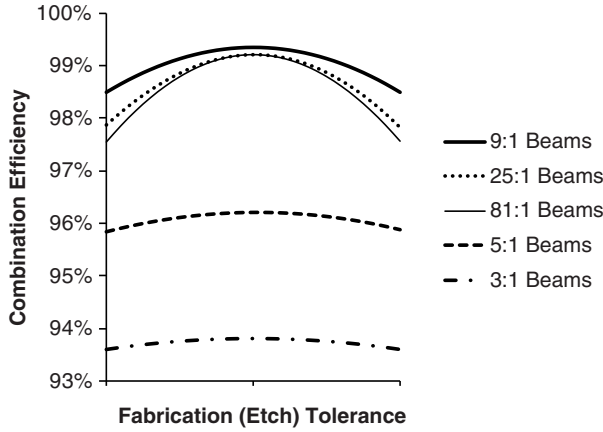


Figure 1.13 Dependence of DOE splitter efficiency on fabrication errors in the surface relief etch depth. The full range of the scale corresponds to typical manufacturing tolerances.

misalignments, the DOE combiner efficiency is then equal to its efficiency as a splitter η_{split} .

A more typical case is when the DOE is used to combine nominally equal power beams, such as generated from an array of identical lasers. In this case, $\sigma_{A(x)} = \sigma_{A(x),D} = 0$, and the BC efficiency is reduced from its limiting value as a splitter to

$$\eta = \eta_{\text{split}} - N\sigma_D^2 = \frac{1}{N} \left(\sum_n |D_n| \right)^2. \quad (1.9)$$

DOE design efficiencies as splitters and as combiners with equal power input beams for a variety of channel counts are shown in Table 1.3. It is notable that even with 20% RMS power split imbalances between channels, Eq. (1.9) predicts that combining efficiency is reduced by only 1% (cf., Figure 1.4). This is a testament to the well-known insensitivity of CBC to power imbalance among channels [8,11].

1.4.2.3 DOE Thermal and Spectral Sensitivity

Since angular dispersion is related to the groove density, the large DOE period results in greatly reduced sensitivity of DOE combiners to thermal distortions or to the input laser linewidths. For the typical case of small diffraction angles, the variation of diffraction angle θ_m with temperature of the DOE is approximately given by

$$\frac{d\theta_m}{dT} = -\alpha \tan(\theta_m) \approx -m\alpha \frac{\lambda}{\Lambda}, \quad (1.10)$$

where α is the thermal expansion coefficient of the DOE substrate. For a typical maximum diffraction angle of $\theta_{N/2} = \pm 25$ mrad (e.g., $N = 50$ beams separated by $\lambda/\Lambda = 1$ mrad in 1D, or $50^2 = 2500$ beams in 2D), one finds the maximum thermally induced angular shift is 1 μ rad for an 80 °C temperature change of an SiO₂ substrate with $\alpha = 0.5$ ppm/°C. This shift is <10% of the natural divergence angle Θ of a

diffraction-limited 10 cm diameter beam. As shown in Table 1.1, the resulting drop in combining efficiency would be substantially less than 1%.

To assess laser power handling, the surface temperature of an HR-coated, 81-beam DOE combiner has been measured under illumination with a 3.6 kW 1064 nm laser. The illuminated area was varied, and intensity of $>20 \text{ kW/cm}^2$ was tolerated without damage. This suggests the DOE beam combination approach is scalable to megawatt-level with a combined beam diameter of $<10 \text{ cm}$. A surface absorption coefficient of $17 \pm 5 \text{ ppm}$ was derived from the observed 3°C steady-state temperature increase of the uncooled, illuminated DOE. A simple 1D thermal analysis of a back-cooled, 5 mm thick, silica DOE shows that with 20 ppm absorption and 10 kW/cm^2 irradiance, the DOE surface temperature rise is only 7°C . This temperature change is more than an order of magnitude below the level at which thermal aberrations are expected to noticeably impact the combination efficiency of 10 cm diameter beams, indicating thermal issues should not limit scaling of this method to megawatt-level powers.

The spectral dispersion of a DOE is also very small and is approximately given by

$$\frac{d\theta_m}{df} = -\frac{\lambda}{c} \tan(\theta_m) \approx -m \frac{\lambda^2}{c\Lambda}, \quad (1.11)$$

which for a maximum diffraction angle of $\theta_{N/2} = \pm 25 \text{ mrad}$ yields $d\theta_{N/2}/df = 0.09 \text{ } \mu\text{rad/GHz}$. Calculations based on Eqs. (1.4) and (1.11) show that for 10 cm beams, dispersion of laser bandwidths of 20 GHz will induce less than 1% impact on combination efficiency. This enables ready use of DOE combiners with $>1 \text{ kW}$ fiber lasers, which require multigigahertz frequency broadening to mitigate power limits from stimulated Brillouin scattering (SBS) [3,47,48].

1.5 High-Power Coherent Beam Combining Demonstrations

This section reviews the design and performance features of coherence-preserving high-power laser amplifiers suitable for integration with the phase control and geometric beam combining technologies described in the previous sections. General features required for the amplifiers are as follows:

- *High power.* For CW laser systems, the cost and complexity involved in CBC phase control and geometric beam combining typically make engineering sense only for scaling well beyond the power limits of the underlying amplifier technologies. As we will discuss subsequently, the present-day combinable CW fiber and free space laser amplifier limits are on the order of ~ 1 and $\sim 10 \text{ kW}$, respectively.
- *High gain.* Low-noise master oscillators are typically limited to subwatt output powers. The available seed power for each amplifier channel is even lower, typically $\sim 1\text{--}10 \text{ mW}$, owing to the attenuation by modulators and distribution splitting to each channel. Hence, amplifier gains often in excess of 50 dB are required to reach kilowatt-level output powers. Since such high levels of

amplification are impractical in a single amplifier stage, this leads to multistage master oscillator power amplifier (MOPA) architectures with gain stages separated by Faraday isolators.

- *High spatial coherence.* As can be seen in Eq. (1.4), CBC efficiency is degraded at $>1\%$ level when intensity-weighted, residual wavefront aberrations exceed 0.1 rad ($\lambda/60$ waves). Hence, each amplifier's output must possess near-perfect beam quality and very low pointing jitter to yield a low-aberration wavefront.
- *High temporal coherence.* Time-dependent phase changes can be imposed by thermal, acoustic, gain, or nonlinear dynamics in each amplifier. Low-frequency phase changes that fall within the servo bandwidth of the phase control system (typically <1 – 10 kHz) can be corrected with high fidelity and do not impact CBC. High-frequency phase changes must be constrained to low levels (again, about <0.1 rad RMS) to avoid impacting CBC efficiency.
- *Polarization.* The amplifier outputs must be copolarized to interfere constructively. Birefringence imposed by the amplifiers must either be kept to small levels or actively compensated.

In Sections 1.5.1 and 1.5.2, we review two laser amplifier technologies – zigzag slabs and fibers – that have been demonstrated to meet these requirements for brightness scaling via CBC. We describe integration of these amplifiers in high-power CBC demonstrations.

1.5.1

Coherent Beam Combining of Zigzag Slab Lasers

In 2009, Northrop Grumman Aerospace Systems demonstrated 105 kW continuous power output with record brightness from a solid-state laser system by coherently combining an array of seven Nd:YAG zigzag slab amplifier chains under the Joint High Power Solid State Laser (JHPSSL) program [5]. The high-stimulated emission cross section of Nd:YAG allowed efficient laser extraction and high amplifier gain with relatively low optical intensities. The consequent low nonlinearity led to outstanding temporal coherence of the amplified beams. The key challenge in this demonstration was maintaining high spatial coherence between amplifiers owing to thermally driven optical wavefront distortions. Low wavefront distortion was achieved through both the slab amplifier design and the use of adaptive optics.

The zigzag slab amplifier geometry shown in Figure 1.14 is, in principle, immune to wavefront distortions from thermal optic path differences (OPDs) [49]. In the zigzag slab concept, a tall, thin, uniformly pumped slab is cooled from both large-area surfaces [50]. Multiple total internal reflections (TIRs) from the cooled surfaces confine to and guide the extracting laser beam down the slab length. Since the extracting beam propagates at an angle relative to the primary thermal gradient, thermal lensing is eliminated as each part of the beam samples the entire slab thickness. The zigzag slab is also far less susceptible to thermal depolarization than other bulk gain architectures [51].

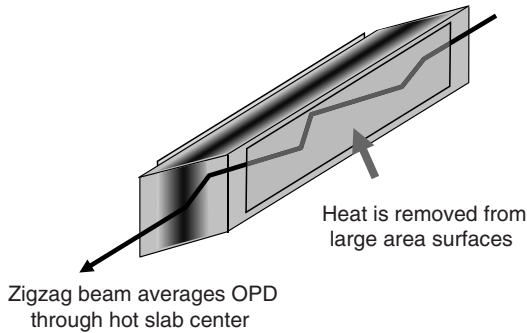


Figure 1.14 Zigzag slab amplifier concept.

In practice, nonuniformities in the slab pumping distribution and surface heat transfer coefficients, as well as edge and end effects, can impose substantial thermal OPD. Figure 1.15 shows a multikilowatt conduction-cooled, end-pumped zigzag slab (CCEPS) gain module that minimizes these effects [52,53]. By injecting diode pump light through the slab tips, the slab itself acts as a homogenizing waveguide as the pump light propagates via TIR down the length of the slab. This provides uniform pump excitation and minimizes any nonuniformities in volumetric heat generation. Careful engineering of a low thermal impedance conductive interface to copper microchannel coolers allows efficient and uniform heat removal. A 2–3 μm thick SiO_2 coating on the cooled faces of the slab contains evanescent fields to ensure near-lossless zigzag propagation of both the pump light and the high-power beam down the slab. The slab has undoped, diffusion-bonded, 45° cut end caps that protrude beyond the coolers to receive focused diode pump light. The high-power

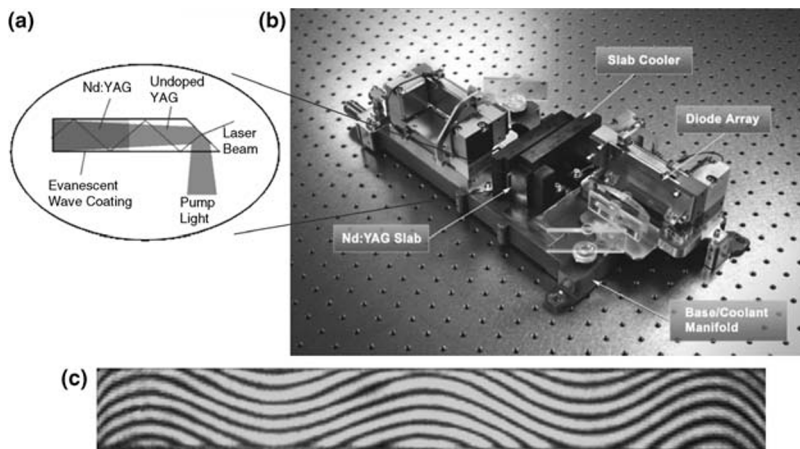


Figure 1.15 (a) CCEPS laser concept. (b) Photo of a 4 kW CCEPS gain module. (c) Typical 4 kW slab OPD measured using a Mach–Zehnder interferometer operating at 658 nm. The zigzag axis is vertical and the nonzigzag axis is horizontal.

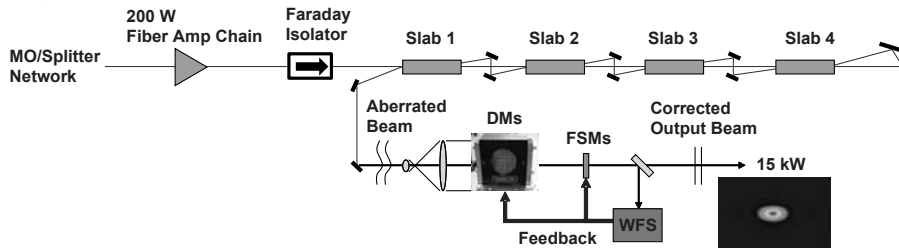


Figure 1.16 Schematic of 15 kW zigzag slab amplifier chain with adaptive optic wavefront correction. The far-field intensity distribution is shown at full power.

beam is injected into the slab at angles that are $20\text{--}30^\circ$ from the normal to the input face to ensure that TIR occurs at the YAG–SiO₂ interface.

To achieve ~ 15 kW power levels, four CCEPS gain modules seeded with an ~ 200 W beam from a fiber amplifier chain were arranged in a double-pass serial configuration, as shown in Figure 1.16 [54,55]. The beam was image relayed from slab to slab to minimize geometric coupling losses. Double-passing each slab via angular multiplexing enabled good saturation and 30% optical extraction efficiency. Angular multiplexing of the slabs was straightforward by choosing different integral numbers of zigzag reflections on each pass [56]. After all eight amplification passes, the beam was amplified to 15 kW.

Despite the advantages of the CCEPS architecture in minimizing thermal aberrations, two or more waves of OPD were imposed on the extracting laser beam for each amplification pass (Figure 1.15c). This OPD arose from small residual pumping/cooling nonuniformities as well as from bulging of the TIR surfaces. Owing to these wavefront aberrations, the 15 kW output beam was unsuitable for coherent combining, necessitating the use of adaptive optics to recover a nearly flat wavefront. As shown in Figure 1.16, the aberrated, high-power beam was expanded to fill the active area of a continuous-facesheet deformable mirror (DM). The tilt was off-loaded to fast steering mirrors (FSMs) to conserve DM stroke and provide high-speed jitter stabilization. High-reflectivity dielectric coatings on the DM and SM enabled use of these elements in the 15 kW beam path. A sample of the output beam was directed to a Shack–Hartmann wavefront sensor (WFS), which generated error signals to drive both adaptive elements in a closed-loop configuration. The corrected output beam had a nearly flat wavefront, with beam quality < 1.3 times the diffraction limit (\times DL) [55].

Since the slab amplifiers naturally produced rectangular, near-flattop beams (Figure 1.17a), they were ideally suited for tiled aperture coherent combining with a high fill factor and relatively low far-field side lobes. The beams from $N=7$ wavefront-corrected MOPA chains were tiled in a close-packed array configuration using scraper mirrors and were phase locked using the OHD phasing technique [20], as shown in Figure 1.5, to form a < 3 times DL, 105 kW composite output beam. The far-field beam profiles displayed in Figure 1.17b and c illustrate the features of coherent beam combination [5,54]. Disabling the phase controller

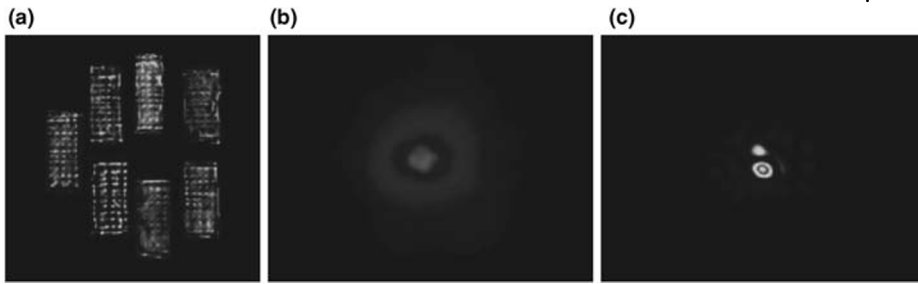


Figure 1.17 100 kW coherently combined beam from seven zigzag slab MOPA chains. (a) Tiled near field. (b) Far field with phasing control disabled. (c) Far field with phasing control enabled.

resulted in only a linear increase of the far-field peak intensity, as N was increased by turning on laser chains. Enabling the phase controller would theoretically increase the far-field intensity by another factor of N . Instead, the observed far-field brightness increased by a factor of 3.8, less than the ideal, owing to the imperfect spatial coherence from residual wavefront aberrations and jitter between amplifier chains.

The entire JHPSSL laser head, comprising the seven-slab MOPA chains and the beam combiner, was packaged in a single water-cooled enclosure with volume $\sim 10\text{ m}^3$ (Figure 1.18 a). The device was continuously operable for periods in excess of 300 s with no thermal degradation (Figure 1.18b). The parallel CBC architecture was essential toward achieving continuous run-times by virtue of distributing waste heat loads among multiple, spatially separated amplifiers. Table 1.4 summarizes the measured performance of the combined system [5]. In principle, brightness can be scaled indefinitely by adding more chains owing to the fully parallel beam tiling and OHD phase control architectures. To our knowledge, this remains the brightest, continuously operable laser system demonstrated to date.

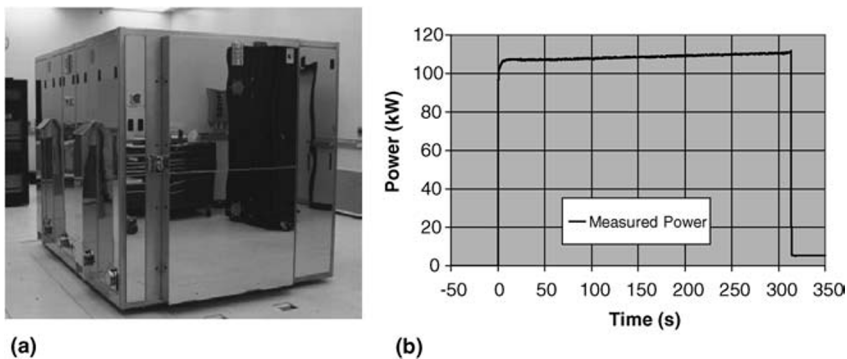


Figure 1.18 (a) 100 kW JHPSSL laser head with seven laser chains and a tiled beam combiner. (b) Output power over the course of a continuous 5 min shot.

Table 1.4 Measured performance of the 100 kW CBC JHPSSL slab laser system.

Parameter	Measured value
Power	105.5 kW
Beam quality	$2.9 \times \text{DL}$
Run-time	313 s
Turn-on time	0.6 s
Electrical efficiency	19.3%

Electrical efficiency is defined as the ratio of CBC output power to diode electrical pump power.

1.5.2

Coherent Beam Combining of Fiber Lasers

While the slab-based JHPSSL system represents a significant advance in solid-state laser power scaling, a CBC array of Yb-doped fiber amplifiers (YDFAs) offers potential for improved efficiency, combined beam quality, and ease of packaging. YDFAs can exhibit optical conversion efficiencies near the quantum limit of $\sim 90\%$ [47], compared to $< 50\%$ typically achieved with bulk gain media. The kilowatt-level multistage fiber amplifiers can generate near-single-mode Gaussian-shaped beams with M^2 beam propagation parameters close to unity, greatly reducing CBC losses due to spatial wavefront aberrations and beam jitter. The mechanical flexibility of fiber gain media allows a high level of packaging and compaction. Ideally, only the free space optics in a CBC fiber system would reside in the beam combiner, where power levels preclude guided wave propagation.

CBC of fibers leads to distinct engineering challenges compared to CBC of slabs. Power levels attainable from modern coherence-preserving fiber amplifiers are an order of magnitude smaller than those from slab lasers, leading to $\sim 10\times$ higher channel counts for comparable power output. Active polarization control may be required, since for typical fiber mode field diameters (MFDs) of tens of micrometers, the waveguide asymmetry of polarization-maintaining (PM) fibers makes single-mode output more difficult to obtain than from non-PM fibers. Finally, the combination of small core sizes, long amplifier lengths, and kilowatt-level power in the fiber can lead to significant nonlinear optical distortion of the seed and consequent loss of temporal coherence. In the remainder of this section, we describe recent experimental and analytic results probing the limits of fiber CBC and review recent demonstrations of high-power fiber CBC.

1.5.2.1 Phase Locking of Nonlinear Fiber Amplifiers

The primary concern for CBC with high-power YDFAs is preserving the temporal, rather than spatial, coherence properties of the MO to allow fully constructive interference of the amplified outputs. The high fiber nonlinearity at kilowatt-level powers makes it critical to avoid fast RIN (i.e., amplitude modulation) on the seed laser. In the presence of RIN, the Kerr nonlinearity (parameterized by the

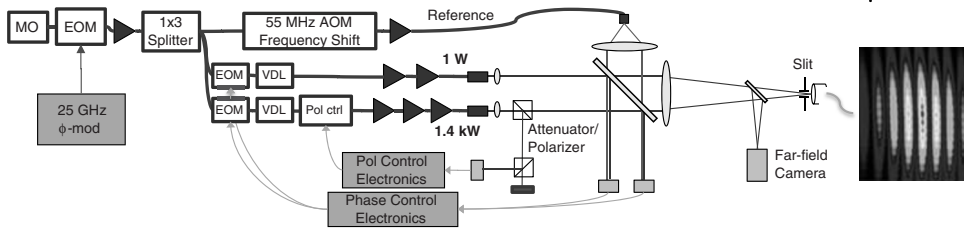


Figure 1.19 Schematic of high-nonlinearity fiber phase locking experiment.

nonlinear refractive index for silica fiber, $n_2 \approx 3 \times 10^{-20} \text{ m}^2/\text{W}$ [57] will induce self-phase modulation (SPM) that may not be correctable with servo loops, degrading the temporal coherence and CBC efficiency [58]. For this reason, actively phase-locked CBC of fiber lasers is often implemented using a single-frequency (SF) MO with low RIN. This avoids the Kerr nonlinearity, but has been limited to $\sim 150 \text{ W}$ per fiber due to SBS [20]. An alternative method that avoids both Kerr nonlinearities and SBS is to broaden the MO linewidth using phase modulation. This has become the standard approach used for high-power CBC fiber demonstrations [21,59,60]. Typical modulation bandwidths range from one to several tens of gigahertz.

The effects of nonlinear temporal decoherence on CBC have been probed by integrating active phase control with a commercial high-power YDFA chain (Figure 1.19) [59]. A SF fiber MO (NP Photonics) operating at a wavelength $\lambda = 1064 \text{ nm}$ was phase modulated using an EOM to broaden the linewidth to 25 GHz FWHM for SBS suppression. Following the EOM, the output was amplified to 100 mW and split into three channels, one of which was frequency shifted by a 55 MHz AOM to serve as an OHD reference for phase locking. Each of the other two channels contained an EOM for piston phase actuation, a manually adjusted variable delay line (VDL) for path matching, and gain-staged YDFAs. The low-power channel contained two PM amplifiers to provide 1 W output power. The high-power channel contained a fiber polarization controller (General Photonics, POS-104) followed by a three-stage, non-PM YDFA chain (IPG Photonics) to boost power to 1.43 kW [48]. The final power amplifier stage was tandem-pumped by high-brightness 1018 nm fiber lasers [3,48]. The outputs from both the high- and low-power fiber amplifier channels were collimated and tiled side by side. The high-power beam was attenuated for amplitude equalization with low-power beam and polarization filtered to provide a feedback signal for the polarization controller. The frequency-shifted reference was combined interferometrically with the 2×1 tiled beam. Separate photodetectors in each channel sensed the phase of the 55 MHz OHD beat notes to provide error signals for phase locking of each beam to the reference with RMS phase fidelity of $\lambda/80$, with resulting beam-to-beam phasing errors of $\Delta\phi_0 = 2^{1/2}(\lambda/80) = 0.11 \text{ rad}$.

The fiber nonlinear phase shift, or *B*-integral, was measured directly by partially amplitude-modulating the MO seed to generate a 100 ns “dark pulse” with 50%

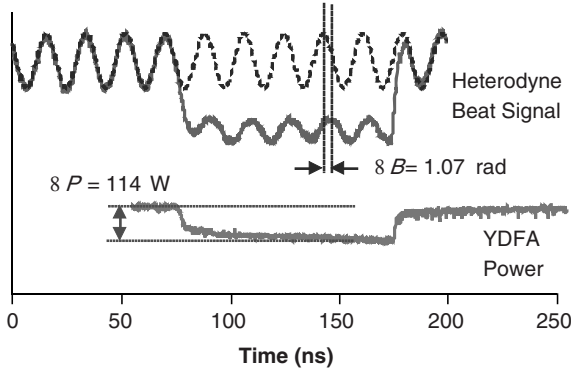


Figure 1.20 Heterodyne measurement of SPM in the high-power fiber amplifier.

lower power (Figure 1.20). This pulse was so fast that it transmitted through the entire amplifier chain without being affected by laser dynamics, and hence there was a substantial, transient drop in the output power ΔP that induced a nonlinear phase shift ΔB due to SPM:

$$\Delta B = \left(\frac{2\pi n_2 L_{\text{eff}}}{\lambda A_{\text{eff}}} \right) \Delta P. \quad (1.12)$$

Here, L_{eff} and A_{eff} are the effective power-weighted fiber length and mode field area, respectively. The term in parentheses in Eq. (1.12) is equivalent to $\Delta B/\Delta P$ and can be determined from the data in Figure 1.20 to be 9.4 ± 1.7 rad/kW from the 1.07 rad phase shift of the 55 MHz heterodyne beat note during the 114 W dark pulse. Hence, the B -integral at full power was $B = (\Delta B/\Delta P) \times 1.43$ kW = 13.4 ± 2.4 rad.

Phase-locking effectiveness was quantified by focusing a low-power sample of the tiled beams onto a far-field camera to generate a stationary fringe pattern (Figure 1.19). A narrow slit whose width is $\sim 5\%$ of a fringe period provided a metric for mutual coherence between the two beams through the visibility [61]:

$$V = (I_{\text{max}} - I_{\text{min}})/(I_{\text{max}} + I_{\text{min}}). \quad (1.13)$$

Here, I_{max} and I_{min} , respectively, are the intensities transmitted through the slit at a peak and a null of the far-field interference pattern, measured sequentially by applying a π -phase shift to the phase controller for one channel. With proper amplitude equalization between the two phase-locked channels, V is equivalent to the mutual coherence between the two beams and is representative of the coherent combining efficiency for coaligned beams.

Figure 1.21a shows V of the phase-locked beam as a function of fiber output power. Tiled aperture and filled aperture measurements yielded similar results within 1%. The low-power data agree with the expected limit based on the accuracy of active phase control [8], $1 - \Delta\phi_0^2 = 1 - (0.11 \text{ rad})^2 = 0.988$. As power was increased to 1.43 kW, V dropped to 0.90. This drop can be attributed to decoherence from SPM. Any RIN faster than the ~ 10 kHz closed-loop OHD phase control

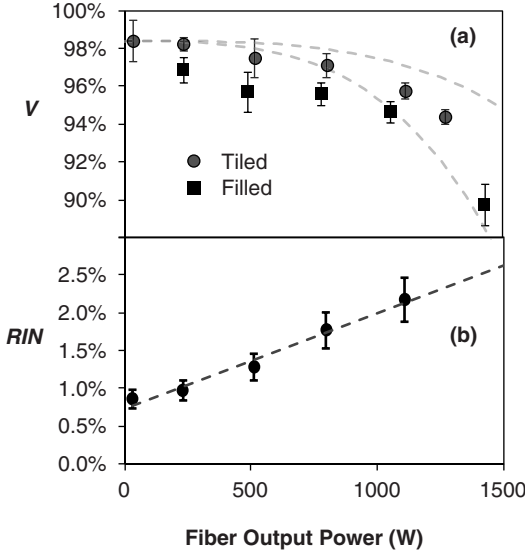


Figure 1.21 (a) Visibility measurements (symbols) and calculated impact of SPM from Eq. (1.14) with propagated uncertainty limits from B and RIN measurements represented by the dashed curves. (b) Measured RIN (symbols) with a linear fit (dashed curve) to provide values for the SPM calculation in (a).

bandwidth (Figure 1.7a) will result in RMS phase noise B -RIN that will be uncorrected and will contribute to decoherence and a drop in V :

$$V = (1 - \Delta\varphi_0^2)[1 - (B \cdot \text{RIN})^2/2]. \quad (1.14)$$

The factor of 2 in Eq. (1.14) arises because only one of the two channels suffers from SPM, so the phase noise variance $(B \cdot \text{RIN})^2$ of the single high-power channel is twice the ensemble phase noise variance of the two-beam array. RIN was measured to be a few percent with 10 kHz–2 GHz detection bandwidth (Figure 1.21b). Based on the measured RIN, the predicted values from Eq. (1.14) agree with the observed decoherence within the propagated uncertainty (Figure 1.21a, dashed curves).

To improve CBC efficiency at these power levels, RIN and/or B must be reduced. Standard noise reduction methods applied to the MO and pump components should enable reduction of RIN to the single percent level. The fiber nonlinearity can likely be reduced substantially by changing the amplifier fiber from tandem pumped to direct diode pumped to increase A_{eff} and decrease L_{eff} .

It is notable that high-efficiency CBC has also been demonstrated recently in pulsed fiber amplifier chains with $B = 38$ rad due to the high peak intensity [62]. This nonlinearity is approximately $3 \times$ greater than that of the 1.4 kW CW amplifier and approaches the threshold for stimulated Raman scattering [57]. Two amplified trains of 1 ns pulses at 25 kHz pulse repetition frequency were combined with 79% efficiency into a single beam with 0.42 mJ pulse energy. Precision matching of

the pulse temporal intensity profiles and amplifier B -integrals was critical in achieving this result. It demonstrates that decoherence from active phase control and fiber nonlinearities are manageable in a CBC system despite the operation deep within the nonlinear regime.

1.5.2.2 Path Length Matching with Broad Linewidths

Owing to the relatively broad linewidths, $\Delta f = 25$ GHz, required for SBS suppression of the 1.4 kW fiber amplifier, optical paths in each amplifier channel must be equalized to a small fraction of the coherence length $L_{\text{coh}} = c/\Delta f$ to prevent significant combining loss due to dephasing [8]. A key question for practical operation of a large array of kilowatt-level fibers is whether the change in fiber path due to thermal expansion and index changes upon turn-on will result in significant dephasing loss. For the 1.4 kW amplifier, this path length change was determined to be approximately 1.5 mm [59]. From Table 1.1, one can calculate that for 25 GHz linewidths, paths must be matched to ± 0.5 mm in order to keep CBC losses below 1%. This is approximately one-third of the turn-on transient, suggesting high-efficiency CBC of an array of such amplifiers would be feasible with modest attention to thermal uniformity between amplifiers.

For even broader linewidths, as may be required for SBS suppression at even higher powers or for CBC of ultrashort pulses [25,63], active controls may be warranted to automate path matching in a servo configuration. Figure 1.22 shows a particularly simple concept for implementing active path matching in a coherent array [64]. Since the accumulated phase errors between the path-mismatched beams are frequency dependent, spectrally filtering the combined output beam serves to optically transduce a group delay error into a frequency-dependent piston phase error. The transduced piston errors can then be nulled by duplicating the closed-loop phase detection electronics, thus bringing the beams into coalignment. It is worth noting that this Fourier domain filtering concept applies to the spatial domain as well, where it can be used for active coherent beam alignments [65].

By choosing the width and separation of the spectral filters in front of the phase and delay sensors, the locking range and precision can accommodate any laser linewidth, even over multiple coherence lengths. Figure 1.23 summarizes test results of simultaneous phase locking and group delay locking on a three-fiber CBC array with a 10.5 nm (2.8 THz) linewidth MO. Independently tunable ~ 1 nm FWHM spectral filters in front of both phase and delay sensors (Figure 1.23a)

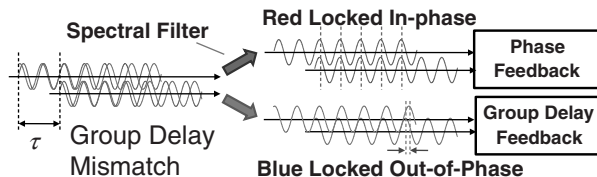


Figure 1.22 Fourier domain filtering concept for coherent detection and control of group delay errors between CBC beams.

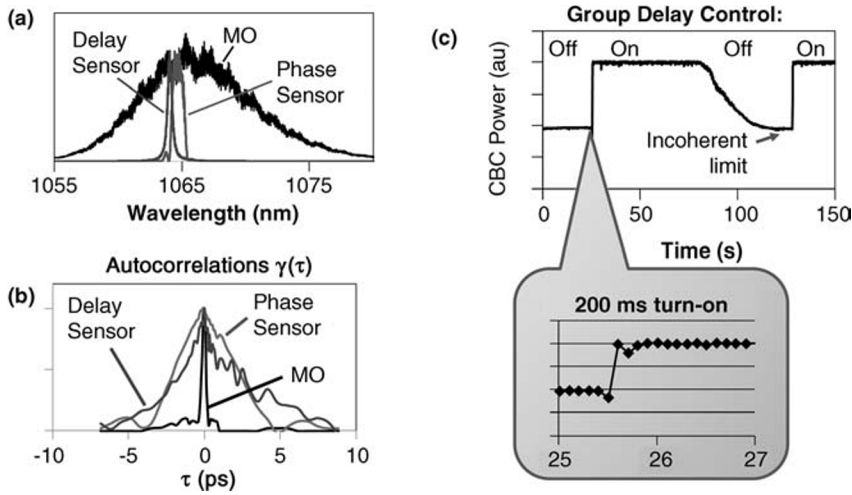


Figure 1.23 Demonstration of simultaneous active phase locking and group delay locking of a three-fiber coherent array. (a) Input and filtered spectra. (b) Linear field autocorrelation envelopes showing increased coherence time of the filtered light. (c) Closed-loop optimization of CBC efficiency when paths are actively controlled.

increased L_{coh} of the detected light from $100\ \mu\text{m}$ to $1\ \text{mm}$ (Figure 1.23b). Starting with fiber mismatches so large that the beams were completely dephased, the fibers were automatically coaligned to an absolute accuracy of $\pm 6\ \mu\text{m}$, within 200 ms of engaging the closed loop (Figure 1.23c). Turning off the closed loop at 80 s in Figure 1.23c resulted in CBC power dropping to the incoherent limit due to fiber thermal drifts, which were corrected upon loop reengagement at 130 s. As long as the mismatches do not exceed the coherence length of the filtered light (which can be arbitrarily increased via narrower spectral filters), the closed loop will be within its control range even when the CBC output beam appears completely decoherent.

1.5.2.3 Diffractive CBC of High-Power Fibers

While the 1.4 kW phasing demonstration already described serves to clarify the nonlinear limitations on CBC of individual fiber amplifiers, a demonstration of actual beam combining requires multiple high-power fiber channels. In this section, we describe two recent demonstrations that highlight the scaling potential of fiber CBC using filled aperture DOE combiners at both high powers and high channel counts. These demonstrations also provide concrete examples of the utility of the perturbative model of Table 1.1 in identifying and quantifying sources of CBC loss.

1.5.2.3.1 CBC of a 1D Fiber Array into a 1.9 kW Beam The highest power demonstration to date of filled aperture beam combining was performed in collaboration with MIT Lincoln Laboratory [66]. A coherent laser array comprised of five 500 W PM fiber amplifier chains was seeded by a common 10 GHz linewidth phase-modulated MO [21]. Each laser chain contained an EOM for piston phase control and a VDL for path

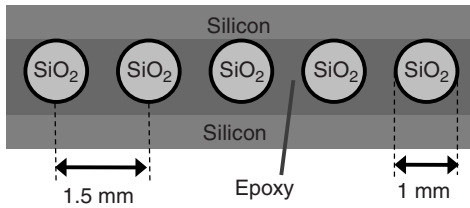


Figure 1.24 End-on face schematic of the Si V-groove exit array.

matching to <1 mm. Each chain's delivery fiber was spliced to a 1 mm diameter end cap and epoxied in a 1.5 mm pitch silicon V-groove array (Figure 1.24). Five adjacent beams from the array were directed onto a five-beam DOE using the Fourier optics geometry shown in Figure 1.12a, with the addition of a monolithic microlens array near the end cap facets that partially collimated each beam to allow an adjustable beam size on the DOE. The collimated Gaussian beam diameter on the DOE was approximately 3.3 mm. The DOE was fabricated on an SiO_2 substrate and was HR coated, with an angular spacing of 8.87 mrad between beams.

The DOE combined most of the incident power into the $m = 0$ diffractive order, with the uncombined power diffracted into higher $|m| > 0$ orders. The DOE was tilted slightly so that the combined beam was reflected outside the plane of diffraction for geometric separation from the input beams. Following the DOE, a loose aperture terminated any residual power left in the $|m| > 0$ orders. A portion of the combined beam was picked off by a beam sampler and sent to diagnostics and a detector to lock the beams in-phase using a hill climbing algorithm [21]. This automatically locked each beam at the DOE input to the conjugate of the phase imposed upon diffraction.

Figure 1.25a shows the combined power in the central $m = 0$ output order as the input power was increased. At low powers, the overall combining efficiency was 90%. This was less than the as-fabricated 96% DOE combining efficiency due to both transverse and rotational mounting errors of the fibers in the V-groove array, as well as a small fraction of output power contained in fiber of higher order modes [8,21]. The combining efficiency dropped near-quadratically with input power to 79% at 2.5 kW.

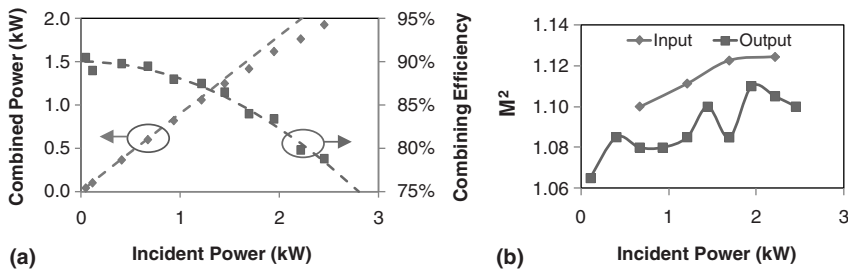


Figure 1.25 Power-dependence of 2.5 kW fiber DOE combining. (a) Combined power and efficiency. The dashed curves are fits to 90% slope efficiency and to Eq. (1.16). (b) Measured M^2 beam parameter.

The $m=0$ output beam was essentially diffraction limited, with $M^2=1.1$ (Figure 1.25b). A slight BQ improvement was seen in comparison to the input beams, which is a consequence of the coherent filtering effect discussed in Section 1.2. Any noncommon aberrations on the incident beams result in decreased combining efficiency as in Eq. (1.4), corresponding to an increase in power in the $|m| > 0$ output orders. This effectively filters out both amplitude and wavefront aberrations, $\delta A_n(x)$ and $\delta \phi_n(x)$, resulting in a near-diffraction-limited $m=0$ output beam. Owing to the space–time symmetry, the same filtering process also serves to clean up the temporal coherence (i.e., reduce time-dependent phase noise) of the output beam when coherently combining nonsingle-frequency lasers.

To diagnose the drop in combining efficiency at high powers, thermal images were recorded of the free space optical components under steady-state illumination at 2.5 kW. DOE heating was $\Delta T < 3^\circ\text{C}$ with peak intensity $> 30\text{ kW/cm}^2$, consistent with the separately measured 17 ppm surface absorption described in Section 1.2. Using Eq. (1.10), the resulting thermal expansion of the DOE would lead to a maximum pointing shift of $(d\theta_m/dT)\Delta T = \pm 30$ nrad for the $m = \pm 2$ diffractive orders. This is ~ 4 orders of magnitude smaller than the diffraction-limited beam divergence of the 3.3 mm diameter beam. Hence, DOE power handling would not be expected to measurably impact CBC efficiency.

Thermal expansion of the fiber V-groove array would be expected to degrade the combining efficiency, since the fiber tip spacing (pitch, x) will no longer match the DOE angles of incidence after the Fourier optics. A maximum surface temperature rise of $\Delta T = 45^\circ\text{C}$ was observed near the fiber tips with input power $P = 2.5$ kW. This suggests a heating coefficient $dT/dP \sim 0.018^\circ\text{C/W}$ at the fiber–end cap interface. As can be seen from Figure 1.24, the undersized Si V-grooves only weakly constrain the fiber positions. Hence, power-dependent changes in pitch $dx/dP = at(dT/dP)$ are dominated by the $t = 500\ \mu\text{m}$ thick interstitial epoxy used to pot the end caps, which has a coefficient of thermal expansion $\alpha = 110\text{ ppm}/^\circ\text{C}$. For small pitch errors $\delta x = (dx/dP)P$, the resulting CBC loss from Table 1.1 is $L = (\sigma_x/w)^2$, where $w = 10\ \mu\text{m}$ is the mode field radius at the delivery fiber tip and σ_x^2 is the mean-square variance of the uniform distribution of tip position errors $\{0, 1, \dots, N-1\} \cdot \delta x$ across the array [67]:

$$\sigma_x = \sqrt{\frac{N^2 - 1}{12}} \delta x. \quad (1.15)$$

This leads to an expected quadratic drop in CBC efficiency $\eta(P)$ with input power:

$$\eta(P) = \eta_0(1 - L) = \eta_0 \left[1 - \frac{N^2 - 1}{12} \left(\frac{at dT}{w dP} \right)^2 P^2 \right], \quad (1.16)$$

where η_0 is the combining efficiency at low power. Equation (1.16) is plotted numerically in Figure 1.25a and agrees with the observed quadratic power dependence and final $\sim 11\%$ drop in CBC efficiency at full power, corresponding to a pitch increase of $\delta x = 2.4\ \mu\text{m}$.

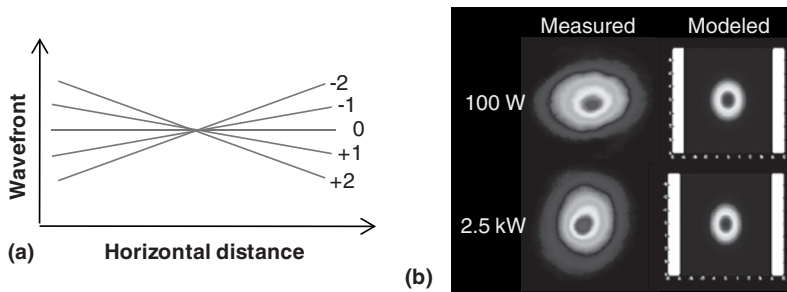


Figure 1.26 (a) Illustration of wavefront tilts across the DOE clear aperture due to thermal expansion of the exit array. (b) Measured and calculated intensity profiles of the CBC beam at the DOE.

Further evidence that thermal growth of the V-groove array is responsible for the drop in combining efficiency can be inferred from the near-field profiles of the combined beam at the DOE (Figure 1.26). As the exit array pitch grows with power, the Fourier lens converts fiber tip positioning errors into wavefront tilts on the DOE. As illustrated in Figure 1.26a, beams can fully interfere constructively only at the center of the DOE near field, since wavefront tilts impose phase errors that grow with distance from the center of the beam. Consequently, the near-field beam footprint of the combined output beam shrinks with power along the grating axis (horizontally in Figure 1.26b). Both measured and modeled beam profiles were consistent with the calculated growth of the exit array.

From these results, it is clear that DOE-based coherent combining is robust at the ~ 2 kW level, with excellent combining efficiency, near-perfect output beam quality, and no indication of reaching DOE power handling limits. The observed drop in combining efficiency with power agreed well with calculations of the thermal expansion of the fiber exit array, which should be amenable to more robustly engineered designs.

1.5.2.3.2 CBC of a 2D Fiber Array into a 0.6 kW Beam The use of multiple DOE orders opens the prospect of utilizing DOE structures that diffract light in two dimensions rather than in one dimension. This effectively squares the number of input orders and provides a means for scaling the number of input beams by one–two orders of magnitude over a linear array generator. Alternatively, for a given number of input beams, a 2D DOE can reduce the angular range of diffractive orders compared to a 1D element, providing added robustness against thermal distortions and enabling coherent combining of broad input linewidths by reducing distortions from angular dispersion. A further practical benefit of 2D DOEs is that more compact and lower aberration optical systems may be used to transform light from a large array of fiber tips onto the DOE.

By superimposing two orthogonal surface relief phase profiles for $1 \times M$ and $1 \times N$ 1D DOE beam splitters, linear patterns can be generated simultaneously in two axes to produce a 2D $M \times N$ grid pattern. For the resulting 2D DOE, the power

splitting efficiency of a single beam into the $(m \times n)$ th order is $D_{m,n}^2 = D_m^2 D_n^2$, where $m = 1 \cdots M$, $n = 1 \cdots N$, and D_m^2 and D_n^2 are the power splitting efficiencies of the underlying 1D DOE designs. It is straightforward to show using Eq. (1.9) that the 2D DOE combining efficiency η_{MN} is simply the product of the underlying efficiencies along each axis:

$$\eta_{MN} = \eta_M \eta_N = \frac{1}{MN} \left(\sum_{m=1}^M D_m \right)^2 \left(\sum_{n=1}^N D_n \right)^2. \quad (1.17)$$

A 15-beam 2D DOE was designed with a surface relief phase profile based on 1D DOE designs with $M=3$ and $N=5$. After fabrication on an SiO_2 substrate, a low-absorption, multilayer dielectric HR coating at 1064 nm was applied. The fabricated DOE was first tested as a splitter to determine its intrinsic efficiency, producing a 3×5 rectangular grid with an angular separation of 8.87 mrad between adjacent beams. The diffraction pattern measured with the DOE used as a splitter is shown in Figure 1.27a, with the central 15 beams overexposed to highlight diffraction of $\sim 10\%$ of the incident power into higher orders. The predicted combining efficiencies for ideal 1×3 and 1×5 DOEs are $\eta_M = 93.8\%$ and $\eta_N = 96.3\%$, respectively, leading to a design efficiency of $\eta_{MN} = 90.3\%$. Based on the measured values for $D_{m,n}^2$ of all 15 beams, the as-fabricated combining efficiency was calculated to be $\eta_{MN} = 87.8\%$ using Eq. (1.17). This is 2.5% less than the design value owing to variations within the manufacturing tolerance range, illustrated in Figure 1.13, that produce a surface shape on the DOE that does not exactly match the design.

The 2D DOE was tested at the Air Force Research Laboratory's (AFRL) Advanced High Power Fiber Laser Testbed in Albuquerque, NM, to demonstrate coherent beam combination [68]. The AFRL Testbed consists of 16~100 W single-frequency Yb-doped fiber amplifiers seeded by a common master oscillator [17] and phase locked using the LOCSET approach [18]. The output of each amplifier was collimated, transmitted through a free space Faraday isolator, and directed onto the DOE with individual steering mirrors in each beam. Due to the layout of the facility, the amplifiers were not equidistant from the DOE, resulting in $\sim 20\%$ RMS mismatches

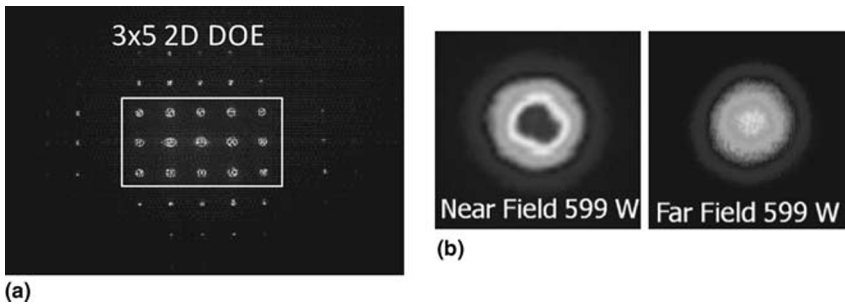


Figure 1.27 (a) Diffraction pattern produced using the 3×5 2D DOE as a beam splitter. (b) Output beam profiles using the 2D DOE as a combiner.

Table 1.5 3×5 2D DOE combining results and analysis.

In (W)	Out (W)	Measured η_{MN} (%)	WFS prediction of η_{MN} (%)
52	38.7	74.5	75.6
684	485	71.0	72.3
885	599	67.7	73.7

in beam sizes at the DOE. Fluctuations in the individual amplifiers limited power measurement accuracy to $\pm 1\%$. Between each measurement, it was necessary to realign and recollimate each of the 15 beams due to thermal beam steering and focusing in the Faraday rotators. Thermal imaging of the DOE surface temperature showed no measurable increase even at full power.

Near-field and far-field images of the combined beam are shown in Figure 1.27b. M^2 of the combined beam was measured to be 1.1 at all power levels. Due to coherent filtering, this is substantially improved over the thermally aberrated input beams, whose M^2 values ranged from 1.1 to 1.4 with an average of 1.26.

Table 1.5 shows CBC results at three different input power levels up to 885 W in all beams. The measured combination efficiencies of ~ 68 –75% were 15–23% lower than expected for ideal beams. To better quantify the sources of loss, after each combination measurement, a Shack–Hartmann WFS captured the wavefront $\phi_{n,m}(x,y)$ and amplitude profiles $|A_{n,m}(x,y)|$ of each individual beam diffracted into the DOE output port. This field data allowed direct calculation of the expected combination efficiency using Eq. (1.2). The predicted values from this calculation are also listed in Table 1.5 and match the measured efficiencies for 52 W and 684 W input powers up to 2%. At the 885 W level, there is an $\sim 6\%$ discrepancy between the measured and predicted efficiencies. Significantly, more thermal steering of the beams was observed at this power level, which, because the WFS data and efficiency measurements were not taken simultaneously, could lead to erroneous predictions due to dynamically varying misalignments.

Further analysis of the WFS data at 684 W, coupled with measurements of the LOCSET servo accuracy [69] and the input polarization extinction ratio, supports the conclusions drawn from the perturbative analysis (Table 1.6). After numerically

Table 1.6 Contributions to η_{MN} at 684 W input power.

Effect	Efficiency (%)	Calculation basis
Intrinsic DOE efficiency	87.8	DOE split ratios
Beam size and BQ	90.8	WFS data
NF and FF beam overlap	90.7	WFS data
Polarization	98	Measured
Piston phasing	>99.5	Estimate
Total calculated η_{MN}	70.5	
Measured η_{MN}	71.0	

removing near-field and far-field centroid overlap errors, the predicted efficiency increased from 72.3 to 79.6%, indicating that both beam centroid overlap and the remaining uncorrected errors (beam size variation and BQ) result in a 9% reduction in efficiency for each effect at this power level. Reducing the aberrations imposed by free space optics through the use of an integrated Fourier telescope combiner, as shown in Figure 1.12a, would be expected to bring combining efficiency closer to the intrinsic DOE limit of $\sim 88\%$. It should be noted that for larger numbers of beams, 2D DOEs are expected to be much more efficient than the 3×5 device demonstrated here. For example, an 81-beam 2D DOE with $M \times N = 9 \times 9$ is ideally expected to be 98.6% efficient, only 0.6% less than the 99.2% efficiency of a linear 1×81 DOE (Table 1.3).

1.5.2.4 CBC of Tm Fibers at 2 μm

In the interest of eye safety, it is desirable to develop laser sources at “retina-safe” wavelengths longer than $1.4 \mu\text{m}$ that are absorbed prior to being focused on the retina. Recent developments have shown Tm-doped fiber amplifiers (TDFAs) emitting in the $2 \mu\text{m}$ region to be a promising avenue for high-power scaling. Notably, an “all-fiber” TDFA has been demonstrated at 1 kW output power [70], highlighting the existence of suitable 790 nm pump diodes and high-power fiber-coupled components at the $2 \mu\text{m}$ wavelength.

For further power scaling via CBC, a 600 W purely single-frequency TDFA has also been demonstrated [71]. The longer lasing wavelength of the TDFA compared to YDFAs increases its SBS threshold through a combination of effects [72], enabling high-coherence SF output without requiring frequency broadening. The TDFA phase noise characteristics were quantified using the self-heterodyne configuration shown in Figure 1.28. Samples of the 600 W amplifier input and output beams were superimposed on a fast photodiode and the resultant electrical signal was passed through an adjustable low-pass filter. The maxima and minima I_{max} and I_{min} of the filtered signals were recorded by manually perturbing the reference fiber to slowly change its optical path length by a few waves, and the fringe visibility V was calculated using Eq. (1.13). Low V for a given cutoff frequency indicates the presence of integrated RMS phase noise σ_ϕ at higher frequencies that is a substantial fraction of a wave, according to the Marechal criterion $V = 1 - \sigma_\phi^2/2$. The factor of 2 is a worst-case assumption that all phase noise originates in the TDFA rather than in the reference arm. As can be seen from Figure 1.28b, $V > 95\%$ above 1 kHz, indicating $\sigma_\phi < 0.3$ rad above this frequency. It can also be seen from Figure 1.28b that phase noise depends only weakly on power. Shutdown of the coolant circulation pumps results in a dramatic decrease in the low-frequency phase noise, indicating the noise is dominated by vibrations coupled to the fiber.

These data indicate that piston phase locking systems with greater than kilohertz-level control bandwidths ought to enable further scaling via coherent combination of multiple fibers. Phase locking of the high-power TDFA output using the OHD technique was demonstrated by installing an AOM frequency shifter and a piezoelectric fiber stretcher in the reference leg of Figure 1.28a. The resulting phase noise

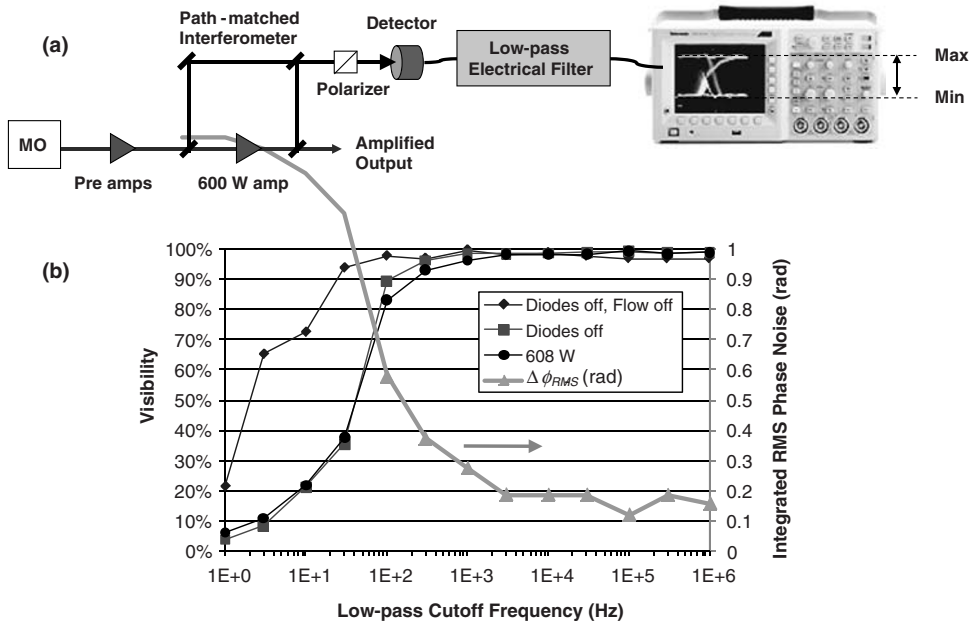


Figure 1.28 (a) Experimental configuration for homodyne fringe visibility measurements. (b) Measured visibility and inferred integrated RMS phase noise.

spectrum is shown in Figure 1.29 a for both open-loop and closed-loop operations at 430 W output (power was limited in these experiments by earlier failure of a diode pump module). Peak noise rejection was ~ 30 dB at low frequencies, and noise was reduced to ~ 10 kHz. The RMS phase noise residuals $\sigma_\phi \approx 0.18$ rad were nearly independent of amplifier power (Figure 1.29b). This performance leads to a predicted coherent combining efficiency of $1 - \sigma_\phi^2 = 97\%$ for a phase-locked array of such amplifiers. It should be noted that either the PM fibers or the active polarization control will be required to ensure constructive interference; both

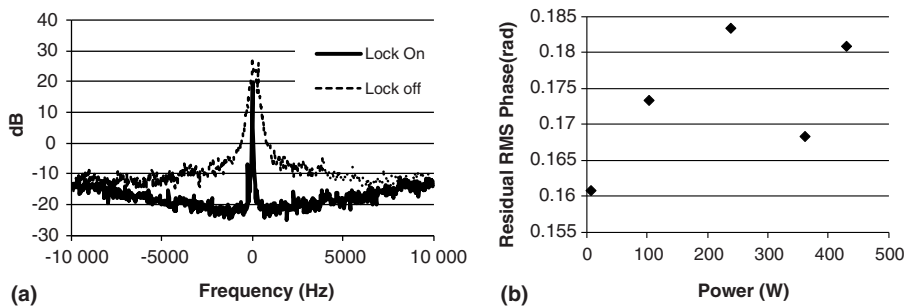


Figure 1.29 (a) Phase noise spectra at 430 W output power. (b) Residual RMS phasing errors with the servo loop engaged.

Table 1.7 Comparison of CBC tolerances between Tm and Yb fibers owing to the $2\times$ longer wavelength.

Parameter	Tm versus Yb	Scaling
Self-phase modulation (nonlinear phase shift, B)	$>8\times$ Better (unrealized potential)	$2\text{--}3\times$ Lower B due to shorter gain lengths $4\times$ Lower B due to larger A_{eff} $2\times$ Lower B due to wavelength
Acoustic-induced phase noise	$2\times$ Better	Half the phase shift as per change in fiber length
Spatial beam alignments	$2\times$ Better	$2\times$ Larger diffraction limit doubles the misalignment tolerance

approaches appear readily extensible to Tm fibers. Recent work at milliwatt-level powers has shown coherent combining of two Tm fiber laser channels using both active and passive phase stabilization approaches [73].

From an engineering perspective, it is interesting to assess tolerances for fiber CBC with wavelength λ as a parameter. This allows a comparison of the relative difficulty of CBC with YDFAs and TDFAs, whose wavelengths are separated approximately by a factor of 2. Without question, doubling λ directly relaxes the tolerances required to coherently overlap the beams as summarized in Table 1.7. The benefits arise from improvements in both spatial and temporal coherences – which scale directly with λ – as well as from a lowering of the fiber nonlinearity B due to the λ -scaling of the fiber transverse waveguide dimension, which increases effective mode field area A_{eff} [cf., Eq. (1.12)]. While the full benefit of fiber A_{eff} scaling is yet to be realized owing to the relative immaturity of the Tm glass material and fiber drawing technology, progress in microstructured Tm-doped photonic crystal fibers [74] provides a technical path forward even in the absence of further material development.

1.6

Conclusion

Advances in the technologies of active phase control, geometric beam combination using diffractive optics, and high-coherence, high-power laser amplifiers have enabled unprecedented high-brightness laser demonstrations through coherent beam combining. CBC has allowed laser developers to replace physical constraints on laser power scaling with more traditional engineering constraints of complexity and cost. To date, tiled CBC of zigzag slab lasers has been demonstrated in excess of 100 kW, which represents not only the highest-power CBC demonstration but also the highest-brightness continuous laser source ever built. Filled aperture CBC of fiber lasers has also been demonstrated near 2 kW. While current CBC fiber powers

are much lower than those from slabs, it appears likely that fiber-based systems will provide substantial benefits in size, weight, efficiency, and packaging despite their lower single-aperture power. Near-term demonstrations of Yb-doped fiber CBC at the 10–100 kW level are in process and appear readily achievable. Recent developments of high-coherence Tm-doped fiber amplifiers at the kilowatt level provide a technology roadmap toward retina-safe CBC laser systems, a key consideration for deployment and propagation through atmosphere.

Acknowledgments

This chapter is mainly the result of the efforts made by many talented and dedicated Northrop Grumman employees over much of the past decade. We would particularly like to express our gratitude to our colleagues Lewis Book, Eric Cheung, James Ho, Hagop Injeyan, Hiroshi Komine, Stuart McNaught, C. C. Shih, Peter Thielen, Mark Weber, Ben Weiss, and Michael Wickham for their many contributions to this work. We would also like to acknowledge our collaborators on the high-power fiber combining experiments, including Angel Flores, Benjamin Pulford, and Anthony Sanchez of the Air Force Research Laboratory and Steve Augst, T.Y. Fan, Shawn Redmond, Dan Ripin, and Charles Yu of MIT Lincoln Laboratory. Finally, we thank the organizations that have supported portions of this work, including the High Energy Laser Joint Technology Office, the US Army Space and Missile Defense Command/Army Forces Strategic Command, the US Air Force, the Defense Advanced Research Projects Agency, and the US Navy.

References

- 1 Hecht, J. (July 2009) Ray guns get real. *IEEE Spectrum*, **46**, 28–33
- 2 Goodno, G.D., Asman, C.P., Anderegg, J., Brosnan, S., Cheung, E.C., Hammons, D., Injeyan, H., Komine, H., Long, W., McClellan, M., McNaught, S.J., Redmond, S., Simpson, R., Sollee, J., Weber, M., Weiss, S.B., and Wickham, M. (2007). Brightness-scaling potential of actively phase-locked solid state laser arrays. *IEEE J. Select. Top. Quantum Electron.*, **13**, 460–472.
- 3 O'Connor, M. and Shiner, B. (2011) High power fiber lasers for industry and defense, in *High Power Laser Handbook* (eds H. Injeyan and G.D. Goodno), McGraw-Hill Professional, New York, pp. 517–532.
- 4 Fan, T.Y. (2005) Laser beam combining for high-power, high-radiance sources. *IEEE J. Select. Top. Quantum Electron.*, **11**, 567–577.
- 5 McNaught, S., Asman, C., Injeyan, H., Jankevics, A., Johnson, A., Jones, G., Komine, H., Machan, J., Marmo, J., McClellan, M., Simpson, R., Sollee, J., Valley, M., Weber, M., and Weiss, S. (2009) 100-kW coherently combined Nd:YAG MOPA laser array. *Frontiers in Optics*, San Jose, CA October 11, 2009, Paper FThD2.
- 6 http://www.as.northropgrumman.com/products/reli/assets/RELI_datasheet.pdf, (accessed May 14, 2012).
- 7 Wacks, M. (2011) Northrop Grumman coherently combined high-power fiber laser for the RELI program. 2nd Annual Advanced High-Power Laser Review, Santa Fe, NM.
- 8 Goodno, G.D., Shih, C.C., and Rothenberg, J.E. (2010) Perturbative analysis of coherent combining efficiency with

- mismatched lasers. *Opt. Express*, **18**, 25403–25414.
- 9 Leger, J.R., Swanson, G.J., and Veldkamp, W.B. (1987) Coherent laser addition using binary phase gratings. *Appl. Opt.*, **26**, 4391–4399.
 - 10 Nabors, C.D. (1994) Effect of phase errors on coherent emitter arrays. *Appl. Opt.*, **33**, 2284–2289.
 - 11 Fan, T.Y. (2009) The effect of amplitude (power) variations on beam combining efficiency for phased arrays. *IEEE J. Select. Top. Quantum Electron.*, **15**, 291–293.
 - 12 Liang, W., Satyan, N., Aflatouni, F., Yariv, A., Kewitsch, A., Rakuljic, G., and Hashemi, H. (2007) Coherent beam combining with multilevel optical phase-locked loops. *J. Opt. Soc. Am. B*, **24**, 2930–2939.
 - 13 Cheung, E.C., Ho, J.G., Goodno, G.D., Rice, R.R., Rothenberg, J., Thielen, P., Weber, M., and Wickham, M. (2008) Diffractive optics-based beam combination of a phase-locked fiber laser array. *Opt. Lett.*, **33**, 354–356.
 - 14 Willke, B., Uehara, N., Gustafson, E.K., Byer, R.L., King, P.J., Seel, S.U., and Savage, R.L. Jr. (1998) Spatial and temporal filtering of a 10-W Nd:YAG laser with a Fabry–Pérot ring-cavity premode cleaner. *Opt. Lett.*, **23**, 1704–1706.
 - 15 Tünnermann, H., Pödl, J.H., Neumann, J., Kracht, D., Willke, B., and Weßels, P. (2011) Beam quality and noise properties of coherently combined ytterbium doped single frequency fiber amplifiers. *Opt. Express*, **19**, 19600–19606.
 - 16 Pupeza, I., Eidam, T., Rauschenberger, J., Bernhardt, B., Ozawa, A., Fill, E., Apolonski, A., Udem, T., Limpert, J., Alahmed, Z.A., Azeze, A.M., Tünnermann, A., Hänsch, T.W., and Krausz, F. (2010) Power scaling of a high-repetition-rate enhancement cavity. *Opt. Lett.*, **35**, 2052–2054.
 - 17 Wagner, T.J. (2012) Fiber laser beam combining and power scaling progress: Air Force Research Laboratory Laser Division. *Proc. SPIE*, **8237**, 823718.
 - 18 Shay, T.M. (2006) Theory of electronically phased coherent beam combination without a reference beam. *Opt. Express*, **14**, 12188–12195.
 - 19 Zhou, P., Liu, Z., Wang, X., Ma, Y., Ma, H., Xu, X., and Guo, S. (2009) Coherent beam combining of fiber amplifiers using stochastic parallel gradient descent algorithm and its application. *IEEE J. Select. Top. Quantum Electron.*, **15**, 248–256.
 - 20 Anderegg, J., Brosnan, S., Cheung, E., Epp, P., Hammons, D., Komine, H., Weber, M., and Wickham, M. (2006) Coherently coupled high-power fiber arrays, in *Fiber Lasers III: Technology, Systems, and Applications, Proceedings of SPIE* (eds A.J. Brown, J. Nilsson, D.J. Harter, and A. Tünnermann), Society of Photo Optical, p. 61020U–1.
 - 21 Yu, C.X., Augst, S.J., Redmond, S.M., Goldizen, K.C., Murphy, D.V., Sanchez, A., and Fan, T.Y. (2011) Coherent combining of a 4kW, eight-element fiber amplifier array. *Opt. Lett.*, **36**, 2686–2688.
 - 22 Yu, C.X., Kinsky, J.E., Shaw, S.E.J., Murphy, D.V., and Higgs, C. (2006) Coherent beam combining of large number of PM fibres in 2-D fibre array. *Electron. Lett.*, **42**, 1024–1025.
 - 23 O’Meara, T.R. (1977) The multidither principle in adaptive optics. *J. Opt. Soc. Am.*, **67**, 306–314.
 - 24 Bourdon, P., Jolivet, V., Bennai, B., Lombard, L., Goular, D., Canat, G., and Vasseur, O. (2009) Theoretical analysis and quantitative measurements of fiber amplifier coherent combining on a remote surface through turbulence. *Proc. SPIE*, **7195**, 719527.
 - 25 Daniault, L., Hanna, M., Lombard, L., Zaouter, Y., Mottay, E., Goular, D., Bourdon, P., Druon, F., and Georges, P. (2011) Coherent beam combining of two femtosecond fiber chirped-pulse amplifiers. *Opt. Lett.*, **36**, 621–623.
 - 26 Ma, Y., Zhou, P., Wang, X., Ma, H., Xu, X., Si, L., Liu, Z., and Zhao, Y. (2010) Coherent beam combination with single frequency dithering technique. *Opt. Lett.*, **35**, 1308–1310.
 - 27 Ma, Y., Zhou, P., Wang, X., Ma, H., Xu, X., Si, L., Liu, Z., and Zhao, Y. (2011) Active phase locking of fiber amplifiers using sine–cosine single-frequency dithering technique. *Appl. Opt.*, **50**, 3330–3336.

- 28 Levy, J. and Roh, K. (1995) Coherent array of 900 semiconductor laser amplifiers. *Proc. SPIE*, **2382**, 58–69.
- 29 Vorontsov, M.A. and Sivokon, V.P. (1998) Stochastic parallel-gradient-descent technique for high-resolution wave-front phase-distortion correction. *J. Opt. Soc. Am. A*, **15**, 2745–2758.
- 30 Weyrauch, T., Vorontsov, M.A., Carhart, G. W., Beresnev, L.A., Rostov, A.P., Polnau, E. E., and Liu, J.J. (2011) Experimental demonstration of coherent beam combining over a 7km propagation path. *Opt. Lett.*, **36**, 4455–4457.
- 31 Redmond, S.M., Creedon, K.J., Kansky, J. E., Augst, S.J., Missaggia, L.J., Connors, M. K., Huang, R.K., Chann, B., Fan, T.Y., Turner, G.W., and Sanchez-Rubio, A. (2011) Active coherent beam combining of diode lasers. *Opt. Lett.*, **36**, 999–1001.
- 32 Redmond, S.M. (2011) Active coherent combination of >200 semiconductor amplifiers using a SPGD algorithm. CLEO:2011 – Laser Applications to Photonic Applications, Paper CTuV1.
- 33 Andrews, J.R. (1989) Interferometric power amplifiers. *Opt. Lett.*, **14**, 33–35.
- 34 Dong, H., Li, X., Wei, C., He, H., Zhao, Y., Shao, J., and Fan, Z. (2009) Coaxial combination of coherent laser beams. *Chin. Opt. Lett.*, **7**, 1012–1014.
- 35 Uberna, R., Bratcher, A., and Tiemann, B. G. (2010) Coherent polarization beam combination. *IEEE J. Quantum Electron.*, **46**, 1191–1196.
- 36 Nelson, B.E., Shakir, S.A., Culver, W.R., Starcher, Y.S., Hedrick, J.W., and Bates, G. M. (2010) System and method for combining multiple fiber amplifiers or multiple fiber lasers. U.S. Patent Appl. 2010/0195195.
- 37 Bruesselbach, H., Jones, D.C., Mangir, M. S., Minden, M., and Rogers, J.L. (2005) Self-organized coherence in fiber laser arrays. *Opt. Lett.*, **30**, 1339–1341.
- 38 Christensen, S.E. and Koski, O. (2007) 2-Dimensional waveguide coherent beam combiner. Advanced Solid-State Photonics, Paper WC1.
- 39 Uberna, R., Bratcher, A., Alley, T.G., Sanchez, A.D., Flores, A.S., and Pulford, B. (2010) Coherent combination of high power fiber amplifiers in a two-dimensional re-imaging waveguide. *Opt. Express*, **18**, 13547–13553.
- 40 Leger, J., Swanson, G.J., and Veldkamp, W. B. (1986) Coherent beam addition of GaAlAs lasers by binary phase gratings. *Appl. Phys. Lett.*, **48**, 888.
- 41 Jain, A., Andrusyak, O., Venus, G., Smirnov, V., and Glebov, L. (2010) Passive coherent locking of fiber lasers using volume Bragg gratings. *Proc. SPIE*, **7580**, 75801S-1–75801S-9.
- 42 Lumeau, J., Glebova, L., and Glebov, L.B. (2011) Near-IR absorption in high-purity photothermorefractive glass and holographic optical elements: measurement and application for high-energy lasers. *Appl. Opt.*, **50**, 5905–5911.
- 43 Dammann, H. and Gortler, K. (1971) High-efficiency in-line multiple imaging by means of multiple phase holograms. *Opt. Commun.*, **3**, 312–315.
- 44 Hergenhan, G., Lücke, B., and Brauch, U. (2003) Coherent coupling of vertical-cavity surface-emitting laser arrays and efficient beam combining by diffractive optical elements: concept and experimental verification. *Appl. Opt.*, **42**, 1667–1680.
- 45 Madasamy, P., Jander, D., Brooks, C., Loftus, T., Thomas, A., Jones, P., and Honea, E. (2009) Dual-grating spectral beam combination of high-power fiber lasers. *IEEE J. Select. Top. Quantum Electron.*, **15**, 337–343.
- 46 Augst, S.J., Lawrence, R.C., Fan, T.Y., Murphy, D.V., and Sanchez, A. (2008) Characterization of diffraction gratings for use in wavelength beam combining at high average power. Frontiers in Optics 2008, Rochester, NY, October 19, 2008, Paper FWG2.
- 47 Khitrov, V., Farley, K., Leveille, R., Galipeau, J., Majid, I., Christensen, S., Samson, B., and Tankala, K. (2010) kW level narrow linewidth Yb fiber amplifiers for beam combining. *Proc. SPIE*, **7686**, 76860.
- 48 Shkurikhin, O., Gapontsev, V., and Platonov, N. (2009) Narrow-linewidth kilowatt-class cw diffraction-limited fiber lasers and amplifiers. 22nd Annual Solid State and Diode Laser Technology Review, Newton, MA.

- 49 Injeyan, H. and Goodno, G.D. (2011) Zigzag slab lasers, in *High Power Laser Handbook* (eds H. Injeyan and G.D. Goodno), McGraw-Hill Professional, New York, pp. 187–205.
- 50 Martin, W.S. and Chernoch, J.P. (1972) Multiple internal reflection face-pumped laser. U.S. Patent No. 3,633,126.
- 51 Ying, C., Bin, C., Patel, M.K.R., and Bass, M. (2004) Calculation of thermal-gradient-induced stress birefringence in slab lasers-I. *IEEE J. Quantum Electron.*, **40**, 909–916.
- 52 Goodno, G.D., Palese, S., Harkenrider, J., and Injeyan, H. (2001) Yb:YAG power oscillator with high brightness and linear polarization. *Opt. Lett.*, **26**, 1672–1674.
- 53 Injeyan, H. and Hoefler, C.S. (2000) End pumped zig-zag slab laser gain medium. U.S. Patent No. 6,094,297.
- 54 Goodno, G.D., Komine, H., McNaught, S.J., Weiss, S.B., Redmond, S., Long, W., Simpson, R., Cheung, E.C., Howland, D., Epp, P., Weber, M., McClellan, M., Sollee, J., and Injeyan, H. (2006) Coherent combination of high-power, zigzag slab lasers. *Opt. Lett.*, **31**, 1247–1249.
- 55 Redmond, S., McNaught, S., Zamel, J., Iwaki, L., Bammert, S., Simpson, R., Weiss, S.B., Szot, J., Flegal, B., Lee, T., Komine, H., and Injeyan, H. (2007) 15 kW Near-diffraction-limited single-frequency Nd:YAG laser. Conference on Lasers and Electro-Optics/Quantum Electronics and Laser Science, Paper CTuHH5.
- 56 Kane, T.J., Kozlovsky, W.J., and Byer, R.L. (1986) 62-dB-Gain multiple-pass slab geometry Nd:YAG amplifier. *Opt. Lett.*, **11**, 216–218.
- 57 Agarwal, G.P. (2007) *Nonlinear Fiber Optics*, 4th edn, Academic Press, New York.
- 58 Goodno, G.D. and Rothenberg, J.E. (2008) Advances and limitations in fiber beam combination. OSA Annual Meeting, Paper FTuW1.
- 59 Goodno, G.D., McNaught, S.J., Rothenberg, J.E., McComb, T., Thielen, P.A., Wickham, M.G., and Weber, M.E. (2010) Active phase and polarization locking of a 1.4-kW fiber amplifier. *Opt. Lett.*, **35**, 1542–1544.
- 60 Jones, D.C. and Scott, A.M. (2007) Characterisation and stabilising dynamic phase fluctuations in large mode area fibres. *Proc. SPIE*, **6453**, 64530Q.1–64530Q.10.
- 61 Goodman, J.W. (2000) *Statistical Optics*, Wiley-Interscience, pp. 163–165.
- 62 Palese, S., Cheung, E., Goodno, G., Shih, C., DiTeodoro, F., McComb, T., and Weber, M. (2012) Coherent combining of pulsed fiber amplifiers in the nonlinear chirp regime with intra-pulse phase control. *Opt. Express*, **20**, 7422–7435.
- 63 Klenke, A., Seise, E., Demmler, S., Rothhardt, J., Breitkopf, S., Limpert, J., and Tünnermann, A. (2011) Coherently-combined two channel femtosecond fiber CPA system producing 3mJ pulse energy. *Opt. Express*, **19**, 24280–24285.
- 64 Weiss, S.B., Weber, M.E., and Goodno, G.D. (2012) Group delay locking of coherently combined broadband lasers. *Opt. Lett.*, **37**, 455–457.
- 65 Goodno, G.D. and Weiss, S.B. (2012) Automated co-alignment of coherent fiber laser arrays via active phase-locking. *Opt. Express*, **20**, 14945–14953.
- 66 Redmond, S.M., Fan, T.Y., Ripin, D.J., Yu, C.X., Augst, S.J., Thielen, P.A., Rothenberg, J.E., and Goodno, G.D. (2012) Diffractive coherent combining of a 2.5-kW fiber laser array into a 1.9kW Gaussian beam. *Opt. Lett.*, **37**, 2832–2834.
- 67 Weisstein, E.W. (2012) Uniform Distribution. From MathWorld, A Wolfram Web Resource, <http://mathworld.wolfram.com/UniformDistribution.html>.
- 68 Thielen, P.A., Ho, J.G., Burchman, D.A., Goodno, G.D., Rothenberg, J.E., Wickham, M.G., Flores, A., Lu, C.A., Pulford, B., Hult, D., Rowland, K.B., and Robin, C. (2012) Two-dimensional diffractive coherent beam combining. Advanced Solid State Photonics, Paper AM3A.2.
- 69 Pulford, B.N. (2011) LOCSET phase locking: operation, diagnostics, and applications, Ph.D. dissertation, University of New Mexico.
- 70 Ehrenreich, T., Leveille, R., Majid, I., Tankala, K., Rines, G., and Moulton, P. (2010) 1 kW all-glass Tm: fiber laser. Photonics West, Session 16, Jan 28, 2010.
- 71 Goodno, G.D., Book, L.D., and Rothenberg, J.E. (2009) Low-phase-noise,

- single-frequency, single-mode 608W thulium fiber amplifier. *Opt. Lett.*, **34**, 1204–1206.
- 72 Goodno, G.D., Book, L.D., Rothenberg, J. E., Weber, M.E., and Weiss, S.B. (2011) Narrow linewidth power scaling and phase stabilization of 2- μm thulium fiber lasers. *Opt. Eng.*, **50**, 111608.
- 73 Zhou, P., Wang, X., Ma, Y., Ma, H., Han, K., Xu, X., and Liu, Z. (2010) Active and passive coherent beam combining of thulium-doped fiber lasers. *Proc. SPIE*, **7843**, 784307.
- 74 Modsching, N., Kadwani, P., Sims, R.A., Leick, L., Broeng, J., Shah, L., and Richardson, M. (2011) Lasing in thulium-doped polarizing photonic crystal fiber. *Opt. Lett.*, **36**, 3873–3875.